



SCUOLA  
ALTI STUDI  
LUCCA

Scuola IMT Alti Studi Lucca

## Phase field modeling of brittle fracture for enhanced assumed strain shells at large deformations: formulation and finite element implementation

Questa è la versione sottoposta a revisione paritaria (postprint) della seguente opera:

*Original*

Phase field modeling of brittle fracture for enhanced assumed strain shells at large deformations: formulation and finite element implementation / Reinoso, J., Paggi, M., Linder, C.. - In: COMPUTATIONAL MECHANICS. - ISSN 0178-7675. - 59:6(2017), pp. 981-1001. [10.1007/s00466-017-1386-3]

*Availability:*

This version is available at: 20.500.11771/3896

*Publisher:*

*Published*

DOI:10.1007/s00466-017-1386-3

*Terms of use:*

This publication is made accessible in accordance with the terms for deposit in the institutional repository, as defined by the IMT School for Advanced Studies Lucca's Open Access Policy. ([https://library.imtlucca.it/sites/default/files/regolamento-policy-open-access-imtlib\\_0.pdf](https://library.imtlucca.it/sites/default/files/regolamento-policy-open-access-imtlib_0.pdf)).

Si prega di consultare le pagine informative dell'editore relative alle politiche di autoarchiviazione.

(Article begins on next page)

# Phase field modeling of brittle fracture for enhanced assumed strain shells at large deformations: formulation and finite element implementation

J. Reinoso · M. Paggi · C. Linder

Received: date / Accepted: date

**Abstract** Fracture of technological thin-walled components can notably limit the performance of their corresponding engineering systems. With the aim of achieving reliable fracture predictions of thin structures, this work presents a new phase field model of brittle fracture for large deformation analysis of shells relying on a mixed enhanced assumed strain (EAS) formulation. The kinematic description of the shell body is constructed according to the solid shell concept. This enables the use of fully three-dimensional constitutive models for the material. The proposed phase field formulation integrates the use of the (EAS) method to alleviate locking pathologies, especially Poisson thickness and volumetric locking. This technique is further combined with the Assumed Natural Strain (ANS) method to efficiently derive a locking-free solid shell element. On the computational side, a fully coupled monolithic framework is consistently formulated. Specific details regarding the corresponding finite element (FE) formulation and the main aspects associated with its implementation in the general purpose packages FEAP and ABAQUS are addressed. Finally, the applicability of the current strategy is demonstrated through several numerical examples involving different loading conditions, and including linear and nonlinear hyperelastic constitutive models.

**Keywords** Shells · Fracture Mechanics · Phase Field Fracture · Finite Elements · Mixed formulation

## 1 Introduction

Many engineering systems are composed of thin-walled structures, whose responses determine and limit the applicability of the corresponding technological components. Applications where shells play a crucial role can be found in aeronautical and aerospace applications as primary structural components (wings and aircraft fuselages) [1], renewable energy systems [2], thermal barrier coatings [3], flexible-electronic systems [4], among others. The prediction and characterization of fracture in thin-walled structures has been a subject of major investigation due to its notable importance. As a consequence of the complex geometric definition, the use of analytical methods for the estimation of such events provide rather

---

J.Reinoso

Elasticity and Strength of Materials Group, School of Engineering, University of Seville, Camino de los Descubrimientos s/n, 41092, Seville, Spain

Tel.: +34 954 487 299

Fax: +34 954 461 637

E-mail: jreinoso@us.es

M. Paggi

IMT School for Advanced Studies Lucca, Piazza San Francesco 19, 55100 Lucca, Italy

Tel.: +39 0583 4326 604

Fax: +39 0583 4326 565

E-mail: marco.paggi@imtlucca.it

C. Linder

Department of Civil and Environmental Engineering, Stanford University, Stanford, CA 94305, USA

Tel.: +01 650 723 2918

Fax: +01 650 723 7514

E-mail: linder@stanford.edu

limited capabilities, and therefore numerical techniques emerge as potential strategies, which lead to a more versatile and general range of analysis.

Within the context of computational procedures for triggering fracture and damage in solids, several formulations relying on different computational techniques have been developed in the last years, see [5, 6, 7, 8, 9, 10, 11, 12, 13, 14, 15] among many others. Specifically for thin-walled structures, several formulations based on the partition of unity (PU) concept have been proposed [16, 17, 18, 20]. The vast majority of current PU formulations assumed the so-called classic shell theories, namely the Kirchhoff-Love (3-parameters) and the Reissner-Mindlin (5-parameters) models for their kinematic descriptions [17, 18, 19, 20]. Subsequently, a phantom-node method was developed considering an arbitrary through the thickness crack normal to the shell-midsurface [21, 22], see also [23] and the references therein given. Further contributions have been also accounted for the use of non-local or gradient enhanced damage approaches [13, 7, 15] with the aim of preventing the well-known mesh dependence pathologies. In this regard, the recent model elaborated by Hosseini and co-authors [24] for solid shells relied on the formulation outlined in [7], but using the underlying continuous kinematic description developed in [23], which embodied an extra kinematic degree of freedom at the centre of the shell thickness. Though these methodologies have been successfully applied to a wide range of applications, most of them present serious difficulties for simulating brittle fracture events.

In order to overcome this limitation, recent phase field methods have been extensively employed for the simulation of fracture in solids [25, 26, 27, 28]. This methodology can be rooted in the classical brittle fracture approach of Griffith and Irwin [29], in which the material failure is attained when a specific energetic criterion is satisfied in terms of the critical energy-release rate (fracture toughness)  $\mathcal{G}_c$ . One of the main ingredients of phase field models of brittle fracture is the idealization of a diffusive crack topology, which introduces the characteristic length of the problem within the variational formulation. This model can be therefore categorized within the gradient damage theory leading to a smeared crack representation since discontinuities in the geometric and kinematics description of the problem are not explicitly considered [8, 7, 13]. Remarkable investigations in this regard are those recently conducted by of Miehe and co-workers [30, 31], where a thermodynamically consistent framework was outlined [32].

At present, a wide number of the existing phase fields models of fracture have been focused on the infinitesimal deformation setting and using displacement-based element archetypes. Recent investigations exploited the practicability of the formulation to large deformation analysis and multi-physics applications [33, 34, 37, 35, 36] and dynamic analyses [38, 39, 40], showing the high potential of this methodology. A summary of the recent progress on phase field fracture is provided in the special issue [41]. However, the use of phase field methods for shells is relatively limited. First attempts have been recently proposed in [42, 43] for geometrically linear problems. In this regard, Miehe and coauthors [43] restricted their developments to standard finite elements based on the Reissner-Midlin theory, which allows the use of standard  $C^0$ -continuous *shape* functions and can be easily incorporated into standard (research and commercial) FE codes. Conversely, Amiri et al. [42] employed Local Maximum-Entropy (LME) meshfree approximations, which require  $C^1$ -continuous basis functions and are difficult to be adapted to standard FE-based packages. Alternative formulations using solid shells and Kirchhoff-Love formulations have been recently proposed for brittle and ductile fracture [44, 45, 46].

In this work, we present a phase field model of brittle fracture for large deformation analysis of thin-walled structures using an enhanced strain-based formulation. In contrast to previous developments, the current shell parametrization is based on the so-called 6-parameter shell model [47]. In particular, we adopt the popular solid shell description of the shell kinematics that is associated with the parametrization of the top and ~~and~~ the bottom surfaces of the body. Thus, starting with the standard displacement-based approach, the first-order (in terms of displacement interpolation) solid shell approach features an identical discretization to that corresponding to standard 8-node brick elements [48, 66, 50].

The potential locking pathologies are remedied by means of the two popular numerical techniques: (1) the Enhanced Assumed Strain (EAS) method, which employs the Hu-Washizu multi-field variational principle as basic result for its derivation [51, 52] and, (2) the Assumed Natural Strain (ANS) [53, 54] method. In line with many advanced shell formulations, the EAS method is herein used to tackle volumetric and Poisson thickness locking effects, whereas the ANS technique is used to alleviate transverse shear and trapezoidal locking deficiencies. Note that within the context of phase field model of brittle fracture, the highly dense FE meshes used to accurately capture the damage variable evolution induces the minor role of membrane and in-plane shear locking. However, as was conceptually suggested in [55], non negligible Poisson thickness and volumetric locking effects are still present. Relying on the previous

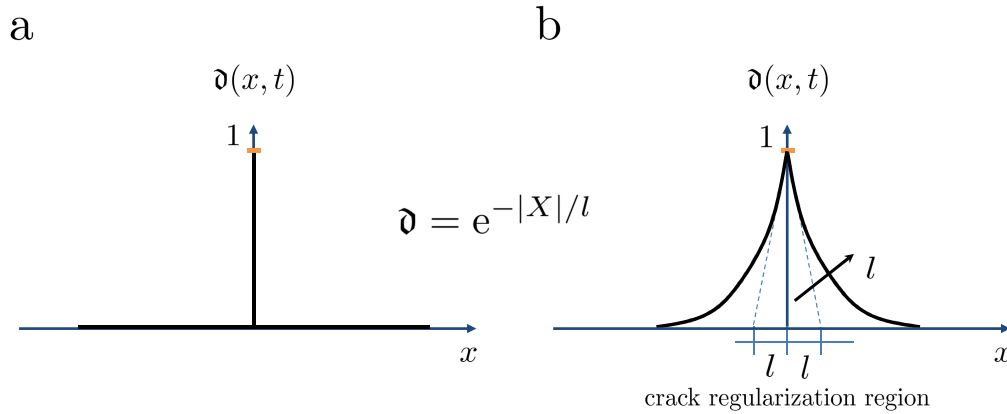


Fig. 1: Sharp and diffusive crack representation. (a) Sharp crack at  $x = 0$ . (b) Diffusive crack at  $x = 0$  whose regularization region depends on the length scale parameter  $l$ .

considerations, the central result of the current investigation concerns the development of a coupling scheme between the phase field model of brittle fracture and mixed FE formulations (particularly for the EAS method) within a large deformation context. In this setting, from the computational standpoint, a fully coupled modeling framework is accordingly developed, whereby the internal degrees of freedom employed for enhancing the strain space can be condensed out at the element level [51]. Consequently, the original structure of the coupling between the phase field and the mechanical field is preserved.

The paper is organized as follows. Section 2 outlines the principal aspects of the phase field modeling approach to brittle fracture. The fundamentals of the solid shell model are given in Section 3. The variational formulation and specific details of the corresponding FE implementation are addressed in Section 4. Section 5 describes the constitutive models used in the present study and specific details with regard to the numerical implementation into the FE packages FEAP and ABAQUS. The assessment of the proposed model through a set of representative numerical applications is presented in Section 6. Finally, the main conclusions of this investigation are drawn in Section 7.

## 2 Fundamentals of the phase field modeling of brittle fracture

This section briefly summarizes the thermodynamically consistent phase field approach of brittle fracture proposed in [30, 31], which can be seen as a non-local continuous damage formulation rooted in the Griffith and Irwin theory of fracture.

The current analysis is focused on a three dimensional setting. Thus, let  $\mathcal{B}_0 \subset \mathbb{R}^3$  define the reference placement of the shell body and  $\mathcal{B}_t \subset \mathbb{R}^3$  its corresponding current configuration. The position vectors at the reference and current configurations are denoted by  $\mathbf{X}$  and  $\mathbf{x}$ , respectively. The body undergoes a motion  $\varphi(\mathbf{X}, t) : \mathcal{B}_0 \times [0, t] \rightarrow \mathbb{R}^3$ , where  $[0, t]$  is the time step interval that maps the reference material points ( $\mathbf{X} \in \mathcal{B}_0$ ) onto the current material points ( $\mathbf{x} \in \mathcal{B}_t$ ), such that  $\mathbf{x} = \varphi(\mathbf{X}, t)$ . We recall the definition of the displacement-derived deformation gradient as  $\mathbf{F}^u := \partial_{\mathbf{X}} \varphi(\mathbf{X}, t)$ , where  $J^u = \det[\mathbf{F}^u]$  is the corresponding Jacobian of the transformation, and  $\partial_{\mathbf{X}}$  denotes the partial derivative with respect to the reference frame.

The key idea of the phase field modeling of brittle fracture consists of regularizing the sharp crack topology within a diffusive crack zone of width  $l$ , which leads to the definition of the scalar-valued function  $\mathfrak{d}$ , with  $\mathfrak{d} : \mathcal{B}_0 \times [0, t] \rightarrow [0, 1]$  [32]. This regularization parameter smears out the sharp crack by a diffusive crack topology within a regularization region whose width depends on  $l$  [30, 31], see the schematic representation for one-dimensional problem in Fig. 1. Thus, this length scale controls the transition between fully intact and broken material points. Within this modeling framework,  $\mathfrak{d}$  is assumed to be a smooth function of  $(\mathbf{X}, t)$  defined in the reference configuration of the body [33], which characterizes for  $\mathfrak{d} = 0$  and  $\mathfrak{d} = 1$  the intact and the cracked states, respectively.

Following Miehe et al, [30] (see also [39]), the equations associated with the phase field problem take the form:

$$\mathfrak{d} - l^2 \Delta \mathfrak{d} = 0 \quad \text{in } \mathcal{B}_0 \quad \text{and} \quad \nabla_{\mathbf{X}} \mathfrak{d} \cdot \mathbf{n} = 0 \quad \text{in } \partial \mathcal{B}_0 \quad (1)$$

where  $\Delta \mathfrak{d}$  stands for the Laplacian of the phase field, and  $\nabla_{\mathbf{X}} \mathfrak{d}$  identifies the gradient of the phase field in the reference configuration. The crack surface density functional  $\gamma(\mathfrak{d}, \nabla_{\mathbf{X}} \mathfrak{d})$  that accounts for the spatially regularized total crack surface can be expressed as:

$$\Gamma_c(\mathfrak{d}) := \int_{\mathcal{B}_0} \gamma(\mathfrak{d}, \nabla_{\mathbf{X}} \mathfrak{d}) \, d\Omega. \quad (2)$$

The integral introduced in Eq.(2) is defined in the reference configuration of the body, and therefore it can be defined by the level set of the crack in the current configuration [33]. As was thoroughly discussed in [25, 27, 26], Eq.(2) converges to the sharp crack surface  $\Gamma_c$  for the limit  $l \rightarrow 0$ . The particular form of the second-order crack surface density functional per unit volume of the solid reads [39]

$$\gamma(\mathfrak{d}, \nabla_{\mathbf{X}} \mathfrak{d}) = \frac{1}{2l} \mathfrak{d}^2 + \frac{l}{2} |\nabla_{\mathbf{X}} \mathfrak{d}|^2. \quad (3)$$

The previous definition of  $\gamma(\mathfrak{d}, \nabla_{\mathbf{X}} \mathfrak{d})$  allows the approximation of the surface integrals defined on sharp crack surfaces by volume integrals as follows:

$$\int_{\Gamma_c} \mathcal{G}_c \, d\partial\Omega \approx \int_{\mathcal{B}_0} \mathcal{G}_c \gamma(\mathfrak{d}, \nabla_{\mathbf{X}} \mathfrak{d}) \, d\Omega, \quad (4)$$

where  $\mathcal{G}_c$  is the fracture toughness according to the Griffith fracture theory.

The weak form of Eq.(1) can be written as:

$$\int_{\mathcal{B}_0} \left( \frac{1}{l} \delta \mathfrak{d} + l \nabla_{\mathbf{X}}(\delta \mathfrak{d}) \cdot \nabla_{\mathbf{X}} \mathfrak{d} \right) \, d\Omega = 0, \quad \forall \delta \mathfrak{d} \in \mathfrak{W}^{\mathfrak{d}}, \quad (5)$$

where  $\mathfrak{W}^{\mathfrak{d}} = \{\delta \mathfrak{d} \in \mathcal{H}^1(\mathcal{B}_0) \mid \delta \mathfrak{d} = 0 \text{ on } \Gamma_c\}$  identifies the space of admissible test functions for the phase field.

### 3 The 6-parameter shell model: solid shell formulation

The parametrization of the shell body is performed through the use of the solid shell concept, whose fundamental aspects are introduced in the sequel. Complying with the solid shell approach, the position vector of any material point,  $\mathbf{X}$ , can be expressed by points of on the top  $\mathbf{X}_t(\xi^1, \xi^2)$  and bottom surfaces  $\mathbf{X}_b(\xi^1, \xi^2)$  of the shell, see Fig. 2. In the reference configuration, this representation takes the form:

$$\mathbf{X}(\boldsymbol{\xi}) = \frac{1}{2} (1 + \xi^3) \mathbf{X}_t(\xi^1, \xi^2) + \frac{1}{2} (1 - \xi^3) \mathbf{X}_b(\xi^1, \xi^2). \quad (6)$$

The parametric space is defined as:  $\mathcal{A} := \{\boldsymbol{\xi} = (\xi^1, \xi^2, \xi^3) \in \mathbb{R}^3 \mid -1 \leq \xi^i \leq +1; i = 1, 2, 3\}$ , where  $(\xi^1, \xi^2)$  denote the in-plane directions and  $\xi^3$  identifies the thickness direction, with  $H$  representing the initial shell thickness.

This definition also renders the description of the shell body in the current configuration by replacing the reference position vector  $\mathbf{X}$  in Eq.(6) by its corresponding updated vector  $\mathbf{x}$  as

$$\mathbf{x}(\boldsymbol{\xi}) = \frac{1}{2} (1 + \xi^3) \mathbf{x}_t(\xi^1, \xi^2) + \frac{1}{2} (1 - \xi^3) \mathbf{x}_b(\xi^1, \xi^2). \quad (7)$$

Accordingly, after some manipulations [1], the kinematics of the shell body,  $\mathbf{u}(\boldsymbol{\xi})$ , can be expressed as:

$$\mathbf{u}(\boldsymbol{\xi}) := \mathbf{x}(\boldsymbol{\xi}) - \mathbf{X}(\boldsymbol{\xi}) = \mathbf{v}(\xi^1, \xi^2) + \xi^3 \mathbf{w}(\xi^1, \xi^2) \quad (8)$$

where  $\mathbf{v}(\xi^1, \xi^2)$  denotes the displacement of the shell midsurface, whereas  $\mathbf{w}(\xi^1, \xi^2)$  identifies the displacement vector that accounts for the difference between the shell director vector in the reference and in the current configuration, see [47]. Note that the previous kinematic description allows the use of unmodified

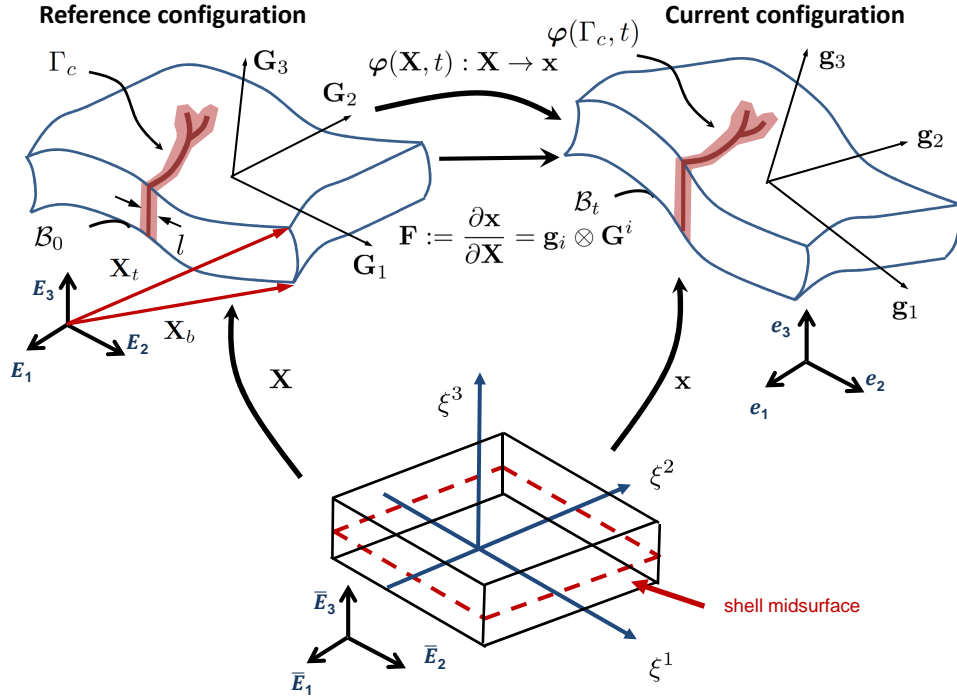


Fig. 2: Definition of reference and current configurations of the shell body, where  $\{\mathbf{E}_i\}_{i=1,3}$ ,  $\{\mathbf{e}_i\}_{i=1,3}$  denote the standard Cartesian frame associated with the reference  $\mathcal{B}_0$  and current  $\mathcal{B}_t$  configurations, respectively. The coordinates  $\boldsymbol{\xi} = \{\xi^1, \xi^2, \xi^3\}$  define the parametric space. Fracture is accounted for through the phase field concept on the surface  $\Gamma_c$ .

three-dimensional constitutive formulations within the corresponding computations. This fact is one of the most appealing aspects of the solid shell formulation herein considered.

The co-variant basis in the reference ( $\mathbf{G}_i$ ) and current ( $\mathbf{g}_i$ ) configurations are defined as:

$$\mathbf{G}_i(\boldsymbol{\xi}) := \frac{\partial \mathbf{X}(\boldsymbol{\xi})}{\partial \xi^i}, \quad \mathbf{g}_i(\boldsymbol{\xi}) := \frac{\partial \mathbf{x}(\boldsymbol{\xi})}{\partial \xi^i}. \quad (9)$$

The dual co- and contra-variant base vectors satisfy the following standard relationships:  $\mathbf{G}_i \cdot \mathbf{G}^j = \delta_i^j$  and  $\mathbf{g}_i \cdot \mathbf{g}^j = \delta_i^j$ . Then, the metric tensors are given as:  $\mathbf{G} = G_{ij} \mathbf{G}^i \otimes \mathbf{G}^j = G^{ij} \mathbf{G}_i \otimes \mathbf{G}_j$ ,  $\mathbf{g} = g_{ij} \mathbf{g}^i \otimes \mathbf{g}^j = g^{ij} \mathbf{g}_i \otimes \mathbf{g}_j$ .

In terms of this curvilinear setting, the displacement derived deformation gradient,  $\mathbf{F}^u$ , reads:

$$\mathbf{F}^u := \mathbf{g}_i \otimes \mathbf{G}^i, \quad (10)$$

whereas the definition of the displacement derived Green-Lagrange deformation tensor takes the following form:

$$\mathbf{E}^u := \frac{1}{2} [(\mathbf{F}^u)^T \mathbf{F}^u - \mathbb{I}_2] = \frac{1}{2} [g_{ij} - G_{ij}] \mathbf{G}^i \otimes \mathbf{G}^j, \quad (11)$$

where  $\mathbb{I}_2$  is the second-order identity tensor in the curvilinear setting. It is worth mentioning that quadratic terms in  $\xi^3$  are generally neglected for thin-walled applications due to their minor contribution [47]. The second Piola-Kirchhoff stress tensor (energetically conjugated to  $\mathbf{E}^u$ ) becomes

$$\mathbf{S} = S^{ij} \mathbf{G}_i \otimes \mathbf{G}_j, \quad (12)$$

where  $S^{ij}$  identify its contravariant components.

With regard to the phase field within the shell body, replicating the definition of the position vectors in the current and reference configuration, a linear interpolation between the top ( $\mathfrak{d}_t$ ) and bottom ( $\mathfrak{d}_b$ ) surfaces of the shell is herein adopted for the phase field variable:

$$\mathfrak{d}(\xi^1, \xi^2, \xi^3) = \frac{1}{2} (1 + \xi^3) \mathfrak{d}_t(\xi^1, \xi^2) + \frac{1}{2} (1 - \xi^3) \mathfrak{d}_b(\xi^1, \xi^2). \quad (13)$$

The ansatz given in Eq.(13) differs from previous formulations with regard to the use of the phase field method to trigger brittle fracture in shells, where a constant value of this magnitude over the shell thickness was proposed [42]. A similar approximation has been recently proposed by Areias and coauthors [45], whereby the use of computational algorithms for element sub-division were also incorporated in order to guarantee the resolution of the crack paths definitions.

#### 4 Variational formulation and finite element discretization

This section outlines the variational formulation of the current model within the context of the mixed Hu-Washizu variational principle to account for the use of the EAS method (Section 4.1) and addresses the corresponding FE formulation (Section 4.2).

##### 4.1 Variational formulation

The objective of this section is to introduce the variational basis of the phase field model for brittle fracture in shells incorporating the use of the EAS method to alleviate locking pathologies. As was previously mentioned, this computational strategy is envisaged principally to remedy Poisson thickness and volumetric locking effects due to the fact that membrane and in-plane locking issues are of minor importance. The minor role of such pathologies stems from the use of very fine in-plane FE discretizations, which are generally required for the adequate application of the phase field modeling framework for brittle fracture applications. Moreover, the current variational formulation can be considered as a fundamental result for the derivation of alternative mixed FE formulations in combination with the phase field approach.

With regard to the enrichment based on the EAS method, in the large deformation setting, two additive schemes have been generally adopted: (1) the pioneering assumed strain formulation proposed by Simo and Armero [52], which modifies the displacement-derived (compatible) deformation gradient ( $\mathbf{F} = \mathbf{F}^u + \tilde{\mathbf{F}}$ , where  $\tilde{\mathbf{F}}$  stands for the incompatible deformation gradient), and (2) the alternative approach developed by Bischoff and Ramm [47], in which the enhancing strain field is additively incorporated into the displacement-derived Green-Lagrange strain tensor. Following the latter method, the complete form of the Green-Lagrange strain tensor reads:  $\mathbf{E} = \mathbf{E}^u + \tilde{\mathbf{E}}$ , where  $\mathbf{E}^u$  and  $\tilde{\mathbf{E}}$  represent the compatible and the incompatible counterparts, respectively.

In the sequel, we outline the variational formulation of the current model whereby the Helmholtz free energy function is expressed in terms on the enhanced definition of the Green-Lagrange strain tensor. Note however that constitutive forms expressed in terms of the deformation gradient,  $\mathbf{F}$ , and the left Cauchy-Green strain tensor,  $\mathbf{b} = \mathbf{F}\mathbf{F}^T$ , can be also employed within the current approach by means of standard operations.

Based on the previous considerations and assuming a scalar-isotropic degradation of the free energy due to the fracture evolution, a modified version of the free-energy function attaining the incorporation of EAS-based finite element archetypes can take the form [33]:

$$\bar{\Psi}(\mathbf{E}^u, \tilde{\mathbf{E}}, \mathfrak{d}) = \mathfrak{g}(\mathfrak{d})\Psi(\mathbf{E}^u, \tilde{\mathbf{E}}), \quad \text{with} \quad \mathfrak{g}(\mathfrak{d}) = [1 - \mathfrak{d}]^2 + \mathcal{K}. \quad (14)$$

In the previous expression, Eq.(14),  $\Psi(\mathbf{E})$  refers to the intact free energy function that also involves the incompatible strain field  $\tilde{\mathbf{E}}$ ;  $\mathfrak{g}(\mathfrak{d})$  stands for the monotonically decreasing degradation function, where  $\mathcal{K} \approx 0$  is a residual positive parameter that prevents numerical instabilities due to fully degraded material response [30].

The point of departure of the current formulation is the multi-field Hu-Washizu variational principle expressed as the stationarity of the following functional of a possibly cracked body:

$$\Pi(\mathbf{S}, \tilde{\mathbf{E}}, \mathbf{u}, \mathfrak{d}) = \int_{\mathcal{B}_0} \mathfrak{g}(\mathfrak{d})\Psi(\mathbf{E}^u, \tilde{\mathbf{E}}) \, d\Omega - \int_{\mathcal{B}_0} \mathbf{S} : \tilde{\mathbf{E}} \, d\Omega + \int_{\mathcal{B}_0} \frac{\mathcal{G}_c l}{2} \left( \frac{\mathfrak{d}^2}{l^2} + |\nabla_{\mathbf{x}} \mathfrak{d}|^2 \right) \, d\Omega + \Pi_{\text{ext}}, \quad (15)$$

where the displacement field ( $\mathbf{u}$ ), the incompatible strain tensor ( $\tilde{\mathbf{E}}$ ), the second Piola-Kirchhoff stress tensor ( $\mathbf{S}$ ) and the phase field variable ( $\vartheta$ ) are the independent variables, and  $\Pi_{\text{ext}}$  identifies the contribution due to the prescribed external actions.

Imposing the standard orthogonality condition between the stress and the incompatible strain fields, the stress field drops out in the subsequent developments [52]. Recalling this condition, the first variation of Eq.(15) with respect to the independent fields  $\tilde{\mathbf{E}}$ ,  $\mathbf{u}$  and  $\vartheta$  leads to the definition of the following continuous multi-field problem:

$$\mathcal{C}^u(\mathbf{u}, \delta\mathbf{u}, \tilde{\mathbf{E}}, \vartheta) = \mathcal{C}_{\text{int}}^u - \mathcal{C}_{\text{ext}}^u = \int_{\mathcal{B}_0} \mathbf{g}(\vartheta) \left[ \frac{\partial \Psi}{\partial \tilde{\mathbf{E}}} : \frac{\partial \mathbf{E}^u}{\partial \mathbf{u}} \delta\mathbf{u} \right] d\Omega + \delta\Pi_{\text{ext}}(\mathbf{u}) = 0, \quad \forall \delta\mathbf{u} \in \mathfrak{V}^u \quad (16)$$

$$\mathcal{C}^{\tilde{\mathbf{E}}}(\mathbf{u}, \tilde{\mathbf{E}}, \delta\tilde{\mathbf{E}}, \vartheta) = \int_{\mathcal{B}_0} \mathbf{g}(\vartheta) \left[ \frac{\partial \Psi}{\partial \tilde{\mathbf{E}}} : \delta\tilde{\mathbf{E}} \right] d\Omega = 0, \quad \forall \delta\tilde{\mathbf{E}} \in \mathfrak{V}^{\tilde{\mathbf{E}}} \quad (17)$$

$$\mathcal{C}^\vartheta(\mathbf{u}, \tilde{\mathbf{E}}, \vartheta, \delta\vartheta) = \int_{\mathcal{B}_0} -2(1 - \vartheta)\delta\vartheta\Psi(\mathbf{E}^u, \tilde{\mathbf{E}}) d\Omega + \int_{\mathcal{B}_0} \mathcal{G}_{cl} \left[ \frac{1}{l^2} \vartheta\delta\vartheta + \nabla_{\mathbf{x}}\vartheta \cdot \nabla_{\mathbf{x}}(\delta\vartheta) \right] d\Omega = 0, \quad \forall \delta\vartheta \in \mathfrak{V}^\vartheta, \quad (18)$$

where  $\mathfrak{V}^u = \{\delta\mathbf{u} \in [H^1(\mathcal{B}_0)] : \delta\mathbf{u} = \mathbf{0} \text{ on } \partial\mathcal{B}_{0,u}\}$  identifies the space of admissible displacement variations, and  $\mathfrak{V}^{\tilde{\mathbf{E}}} = [L_2(\mathcal{B}_0)]$  stands for the admissible space corresponding to the test functions of the enhanced strain modes.

## 4.2 Finite element formulation

### 4.2.1 Finite element interpolation

The finite element discretization is introduced following standard arguments regarding the isoparametric interpolation concept. Let the initial configuration  $\mathcal{B}_0$  be discretized into  $n_e$  non-overlapping elements, such that  $\mathcal{B}_0 \approx \bigcup_{e=1}^{n_e} \mathcal{B}_0^{(e)}$ . Relying on the solid shell kinematic parametrization (Section 3), we use standard tri-linear shape functions of an eight-node element to interpolate the kinematics and the phase field variable within the element domain. The Lagrangian and the Eulerian geometries are interpolated through standard trilinear shape functions  $N^I$  ( $\mathbf{N}(\boldsymbol{\xi})$  in matrix notation) as

$$\mathbf{X} = \sum_{I=1}^{n_n} N^I(\boldsymbol{\xi})\mathbf{X}_I = \mathbf{N}(\boldsymbol{\xi})\tilde{\mathbf{X}} \quad \text{and} \quad \mathbf{x} = \sum_{I=1}^{n_n} N^I(\boldsymbol{\xi})\mathbf{x}_I = \mathbf{N}(\boldsymbol{\xi})\tilde{\mathbf{x}}, \quad (19)$$

where  $\mathbf{X}_I$  and  $\mathbf{x}_I$  denote the discrete nodal values and  $n_n = 8$  identifies the number of nodes in the reference and in the current configurations, respectively. These nodal values are collected into the respective global vectors  $\tilde{\mathbf{X}}$  and  $\tilde{\mathbf{x}}$  for both configurations.

The interpolation of the displacement field ( $\mathbf{u}$ ), its variation ( $\delta\mathbf{u}$ ) and its increment ( $\Delta\mathbf{u}$ ) can be expressed as:

$$\mathbf{u} \approx \mathbf{N}(\boldsymbol{\xi})\mathbf{d}, \quad \delta\mathbf{u} \approx \mathbf{N}(\boldsymbol{\xi})\delta\mathbf{d}, \quad \Delta\mathbf{u} \approx \mathbf{N}(\boldsymbol{\xi})\Delta\mathbf{d}, \quad (20)$$

where  $\mathbf{d}$  represents the nodal displacement vector at the element level.

Similarly, the compatible strain field ( $\mathbf{E}^u$ ), its variation ( $\delta\mathbf{E}^u$ ) and its increment ( $\Delta\mathbf{E}^u$ ) are interpolated through the displacement-strain  $\mathbf{B}(\mathbf{d})$  operator as

$$\mathbf{E}^u \approx \mathbf{B}(\mathbf{d})\mathbf{d}, \quad \delta\mathbf{E}^u \approx \mathbf{B}(\mathbf{d})\delta\mathbf{d}, \quad \Delta\mathbf{E}^u \approx \mathbf{B}(\mathbf{d})\Delta\mathbf{d}. \quad (21)$$

Specific details with regard to the particular form of the displacement-strain  $\mathbf{B}(\mathbf{d})$  operator are given in A.

The enhancing strain field is interpolated at the element level by means of the operator  $\mathbf{M}(\boldsymbol{\xi})$ , which depends on the number of enhancing modes taken into consideration [66,55]. Based on this concept, the interpolation of the enhanced strain ( $\tilde{\mathbf{E}}$ ), its variation ( $\delta\tilde{\mathbf{E}}$ ) and its increment ( $\Delta\tilde{\mathbf{E}}$ ) are related to the vector  $\boldsymbol{\varsigma}$ , which contains the EAS parameters. Therefore, this interpolation can be expressed as

$$\tilde{\mathbf{E}} \approx \mathbf{M}(\boldsymbol{\xi})\boldsymbol{\varsigma}, \quad \delta\tilde{\mathbf{E}} \approx \mathbf{M}(\boldsymbol{\xi})\delta\boldsymbol{\varsigma}, \quad \Delta\tilde{\mathbf{E}} \approx \mathbf{M}(\boldsymbol{\xi})\Delta\boldsymbol{\varsigma}. \quad (22)$$

The number of EAS parameters and the size of the interpolation matrix  $\mathbf{M}(\boldsymbol{\xi})$  is discussed in Section 4.2.3.

Adopting a similar scheme, the phase field interpolation ( $\vartheta$ ), its variation ( $\delta\vartheta$ ) and its increment ( $\Delta\vartheta$ ) at the element level are given as

$$\vartheta = \mathbf{N}(\boldsymbol{\xi})\bar{\vartheta}, \quad \delta\vartheta = \mathbf{N}(\boldsymbol{\xi})\delta\bar{\vartheta}, \quad \Delta\vartheta = \mathbf{N}(\boldsymbol{\xi})\Delta\bar{\vartheta}, \quad (23)$$

where  $\bar{\vartheta}$  stands for the nodal phase field values. Note that the same shape functions  $\mathbf{N}(\boldsymbol{\xi})$  are considered for the approximation of the kinematics and the phase field variables.

The material gradient of the phase field, its variation and its increment are interpolated through a suitable operator  $\mathbf{B}^\vartheta$  as

$$\nabla_{\mathbf{X}}\vartheta = \mathbf{B}^\vartheta(\boldsymbol{\xi})\bar{\vartheta}, \quad \nabla_{\mathbf{X}}\delta\vartheta = \mathbf{B}^\vartheta(\boldsymbol{\xi})\delta\bar{\vartheta}, \quad \nabla_{\mathbf{X}}\Delta\vartheta = \mathbf{B}^\vartheta(\boldsymbol{\xi})\Delta\bar{\vartheta}. \quad (24)$$

After inserting the discretization process given in Eqs.(19)-(24), the discrete version of the residual equations corresponding to the displacements, the enhancing strains and the phase field variable take the form:

$$\hat{C}^u(\mathbf{d}, \delta\mathbf{d}, \bar{\vartheta}, \boldsymbol{\varsigma}) = \hat{C}_{\text{int}}^u(\mathbf{d}, \delta\mathbf{d}, \bar{\vartheta}, \boldsymbol{\varsigma}) - \hat{C}_{\text{ext}}^u(\mathbf{d}, \delta\mathbf{d}) = \delta\mathbf{d}^T \left[ \int_{\mathcal{B}_0} \mathbf{g}(\vartheta)\mathbf{B}(\mathbf{d})^T \mathbf{S} \, d\Omega \right] - \mathbf{R}_{\text{ext}}^d = \mathbf{R}_{\text{int}}^d - \mathbf{R}_{\text{ext}}^d, \quad (25)$$

$$\hat{C}^{\bar{E}}(\mathbf{d}, \bar{\vartheta}, \boldsymbol{\varsigma}, \delta\boldsymbol{\varsigma}) = \delta\boldsymbol{\varsigma}^T \left[ \int_{\mathcal{B}_0} \mathbf{g}(\vartheta)\mathbf{M}(\boldsymbol{\xi})^T \mathbf{S} \, d\Omega \right], \quad (26)$$

$$\hat{C}^\vartheta(\mathbf{d}, \bar{\vartheta}, \delta\bar{\vartheta}, \boldsymbol{\varsigma}) = \delta\bar{\vartheta}^T \left[ \int_{\mathcal{B}_0} -2(1-\vartheta)\mathbf{N}(\boldsymbol{\xi})^T \Psi(\mathbf{d}, \boldsymbol{\varsigma}) \, d\Omega + \int_{\mathcal{B}_0} \mathcal{G}_{cl} \left[ (\mathbf{B}^\vartheta(\boldsymbol{\xi}))^T \nabla_{\mathbf{X}}\vartheta + \frac{1}{l^2}\mathbf{N}(\boldsymbol{\xi})^T \vartheta \right] \, d\Omega \right]. \quad (27)$$

For subsequent developments, the residual vectors associated with the displacement field, the enhancing strains and the phase field are respectively defined as follows:  $\mathbf{R}^d := \hat{C}^u(\mathbf{d}, \delta\mathbf{d}, \bar{\vartheta}, \boldsymbol{\varsigma}) = \hat{C}_{\text{int}}^u - \hat{C}_{\text{ext}}^u$ ,  $\mathbf{R}^s := \hat{C}^{\bar{E}}(\mathbf{d}, \bar{\vartheta}, \boldsymbol{\varsigma}, \delta\boldsymbol{\varsigma})$ , and  $\mathbf{R}^\vartheta := \hat{C}^\vartheta(\mathbf{d}, \bar{\vartheta}, \delta\bar{\vartheta}, \boldsymbol{\varsigma})$ .

Additionally, in line with [56], the irreversibility of the process is taken into account through the introduction of a history variable in a modified version of the corresponding phase field residual vector given as

$$\mathbf{R}^\vartheta(\mathbf{d}, \bar{\vartheta}, \delta\bar{\vartheta}, \boldsymbol{\varsigma}) = \int_{\mathcal{B}_0} -2(1-\vartheta)\mathbf{N}(\boldsymbol{\xi})^T \left[ \Psi(\mathbf{d}, \boldsymbol{\varsigma}) - \frac{\eta}{n\Delta t} \langle \dot{\bar{\vartheta}} \rangle_-^n \right] \, d\Omega + \int_{\mathcal{B}_0} \mathcal{G}_{cl} \left[ (\mathbf{B}^\vartheta(\boldsymbol{\xi}))^T \nabla_{\mathbf{X}}\vartheta + \frac{1}{l^2}\mathbf{N}(\boldsymbol{\xi})^T \vartheta \right] \, d\Omega \quad (28)$$

where  $\eta$  stands for a penalty parameter that should be chosen with care in order to preserve the right conditioning number of the stiffness matrix,  $n$  is a positive number ( $n = 2$ , see [56]),  $\langle \dot{\bar{\vartheta}} \rangle_-^n = \langle \bar{\vartheta}^{t+1} - \bar{\vartheta}^t \rangle_-^n$  and the operator  $\langle \cdot \rangle_-$  applied to a generic variable  $a$  reads:

$$\langle a \rangle_- = \begin{cases} -a, & a < 0, \\ 0, & a \geq 0. \end{cases} \quad (29)$$

#### 4.2.2 Linearization of the multi-field weak form

The nonlinear character of the multi-field residual equations given in Eqs.(25)-(28) requires the adoption of the incremental-iterative Newton-Raphson solution scheme. The consistent linearization of this system is obtained through the Gateaux directional derivative concept, resulting in

$$\hat{L}[\mathbf{R}^d](\mathbf{d}, \delta\mathbf{d}, \Delta\mathbf{d}, \bar{\vartheta}, \Delta\bar{\vartheta}, \boldsymbol{\varsigma}, \Delta\boldsymbol{\varsigma}) = \mathbf{R}^d(\mathbf{d}, \delta\mathbf{d}, \bar{\vartheta}, \boldsymbol{\varsigma}) + \Delta_{\mathbf{d}}\mathbf{R}^d \Delta\mathbf{d} + \Delta_{\bar{\vartheta}}\mathbf{R}^d \Delta\bar{\vartheta} + \Delta_{\boldsymbol{\varsigma}}\mathbf{R}^d \Delta\boldsymbol{\varsigma} \quad (30)$$

$$\hat{L}[\mathbf{R}^s](\mathbf{d}, \Delta\mathbf{d}, \bar{\vartheta}, \Delta\bar{\vartheta}, \boldsymbol{\varsigma}, \delta\boldsymbol{\varsigma}, \Delta\boldsymbol{\varsigma}) = \mathbf{R}^s(\mathbf{d}, \bar{\vartheta}, \boldsymbol{\varsigma}, \delta\boldsymbol{\varsigma}) + \Delta_{\mathbf{d}}\mathbf{R}^s \Delta\mathbf{d} + \Delta_{\bar{\vartheta}}\mathbf{R}^s \Delta\bar{\vartheta} + \Delta_{\boldsymbol{\varsigma}}\mathbf{R}^s \Delta\boldsymbol{\varsigma} \quad (31)$$

$$\hat{L}[\mathbf{R}^\vartheta](\mathbf{d}, \bar{\mathbf{d}}, \delta\bar{\mathbf{d}}, \Delta\bar{\mathbf{d}}, \boldsymbol{\varsigma}, \delta\boldsymbol{\varsigma}, \Delta\boldsymbol{\varsigma}) = \mathbf{R}^\vartheta(\mathbf{d}, \bar{\mathbf{d}}, \delta\bar{\mathbf{d}}, \boldsymbol{\varsigma}) + \Delta_{\mathbf{d}}\mathbf{R}^\vartheta\Delta\mathbf{d} + \Delta_{\bar{\mathbf{d}}}\mathbf{R}^\vartheta\Delta\bar{\mathbf{d}} + \Delta_{\boldsymbol{\varsigma}}\mathbf{R}^\vartheta\Delta\boldsymbol{\varsigma}, \quad (32)$$

where  $\Delta_*[\bullet]$  denotes the directional derivative operator with respect to the field  $*$ . The linearized system of equations in matrix form is then given as

$$\begin{bmatrix} \mathbf{k}_{dd} & \mathbf{k}_{d\bar{\mathbf{d}}} & \mathbf{k}_{d\boldsymbol{\varsigma}} \\ \mathbf{k}_{\bar{\mathbf{d}}d} & \mathbf{k}_{\bar{\mathbf{d}}\bar{\mathbf{d}}} & \mathbf{k}_{\bar{\mathbf{d}}\boldsymbol{\varsigma}} \\ \mathbf{k}_{\boldsymbol{\varsigma}d} & \mathbf{k}_{\boldsymbol{\varsigma}\bar{\mathbf{d}}} & \mathbf{k}_{\boldsymbol{\varsigma}\boldsymbol{\varsigma}} \end{bmatrix} \begin{bmatrix} \Delta\mathbf{d} \\ \Delta\bar{\mathbf{d}} \\ \Delta\boldsymbol{\varsigma} \end{bmatrix} = \begin{bmatrix} \mathbf{R}_{\text{ext}}^d \\ \mathbf{0} \\ \mathbf{0} \end{bmatrix} - \begin{bmatrix} \mathbf{R}_{\text{int}}^d \\ \mathbf{R}_{\text{int}}^\vartheta \\ \mathbf{R}_{\text{int}}^\varsigma \end{bmatrix} \quad (33)$$

Note that the formulation given in Eq.(33) regards a fully coupled system. A discussion regarding the fully coupled and staggered solution strategies is addressed in Section 6.

The different element tangent operators take the forms:

$$\mathbf{k}_{dd} = \int_{\mathcal{B}_0} [(1 - \vartheta)^2 + \mathcal{K}] \left[ \frac{\partial \mathbf{B}(\mathbf{d})^T}{\partial \mathbf{d}} \mathbf{S} + \mathbf{B}(\mathbf{d})^T \mathbb{C} \mathbf{B}(\mathbf{d}) \right] d\Omega = \mathbf{k}_{dd,\text{geom}} + \mathbf{k}_{dd,\text{mat}}, \quad (34a)$$

$$\mathbf{k}_{d\bar{\mathbf{d}}} = \int_{\mathcal{B}_0} -2(1 - \vartheta) \mathbf{B}(\mathbf{d})^T \mathbf{S} \mathbf{N}(\boldsymbol{\xi}) d\Omega, \quad (34b)$$

$$\mathbf{k}_{d\boldsymbol{\varsigma}} = \int_{\mathcal{B}_0} [(1 - \vartheta)^2 + \mathcal{K}] \mathbf{M}(\boldsymbol{\xi})^T \mathbb{C} \mathbf{B}(\mathbf{d}) d\Omega, \quad (34c)$$

$$\mathbf{k}_{\bar{\mathbf{d}}d} = \int_{\mathcal{B}_0} -2(1 - \vartheta) \mathbf{N}(\boldsymbol{\xi})^T \mathbf{S}^T \mathbf{B}(\mathbf{d}) d\Omega, \quad (34d)$$

$$\mathbf{k}_{\bar{\mathbf{d}}\bar{\mathbf{d}}} = \int_{\mathcal{B}_0} \left[ \frac{\mathcal{G}_c}{l} + 2\psi \right] \mathbf{N}(\boldsymbol{\xi})^T \mathbf{N}(\boldsymbol{\xi}) d\Omega + \int_{\mathcal{B}_0} \mathcal{G}_{cl} (\mathbf{B}^\vartheta(\boldsymbol{\xi}))^T \mathbf{B}^\vartheta(\boldsymbol{\xi}) d\Omega + \int_{\mathcal{B}_0} \frac{\eta}{\Delta t} \left\langle \frac{\dot{\vartheta}}{\vartheta} \right\rangle_-^{n-1} \mathbf{N}(\boldsymbol{\xi})^T \mathbf{N}(\boldsymbol{\xi}) d\Omega, \quad (34e)$$

$$\mathbf{k}_{\bar{\mathbf{d}}\boldsymbol{\varsigma}} = \int_{\mathcal{B}_0} -2(1 - \vartheta) \mathbf{N}(\boldsymbol{\xi})^T \mathbf{S}^T \mathbf{M}(\boldsymbol{\xi}) d\Omega, \quad (34f)$$

$$\mathbf{k}_{\boldsymbol{\varsigma}d} = \int_{\mathcal{B}_0} [(1 - \vartheta)^2 + \mathcal{K}] \mathbf{M}(\boldsymbol{\xi})^T \mathbb{C} \mathbf{B}(\mathbf{d}) d\Omega, \quad (34g)$$

$$\mathbf{k}_{\boldsymbol{\varsigma}\bar{\mathbf{d}}} = \int_{\mathcal{B}_0} -2(1 - \vartheta) \mathbf{M}(\boldsymbol{\xi})^T \mathbf{S} \mathbf{N}(\boldsymbol{\xi}) d\Omega, \quad (34h)$$

$$\mathbf{k}_{\boldsymbol{\varsigma}\boldsymbol{\varsigma}} = \int_{\mathcal{B}_0} [(1 - \vartheta)^2 + \mathcal{K}] \mathbf{M}(\boldsymbol{\xi})^T \mathbb{C} \mathbf{M}(\boldsymbol{\xi}) d\Omega. \quad (34i)$$

Condensing out the enhanced strain field, since no inter-element continuity is required [47], we end up with the final system of equations that preserves the original coupled scheme between the kinematic and the phase field outlined in [56] as

$$\begin{bmatrix} \mathbf{k}_{dd}^* & \mathbf{k}_{d\bar{\mathbf{d}}}^* \\ \mathbf{k}_{\bar{\mathbf{d}}d}^* & \mathbf{k}_{\bar{\mathbf{d}}\bar{\mathbf{d}}}^* \end{bmatrix} \begin{bmatrix} \Delta\mathbf{d} \\ \Delta\bar{\mathbf{d}} \end{bmatrix} = \begin{bmatrix} \mathbf{R}_{\text{ext}}^d \\ \mathbf{0} \end{bmatrix} - \begin{bmatrix} \mathbf{R}_{\text{int}}^{d*} \\ \mathbf{R}_{\text{int}}^{\vartheta*} \end{bmatrix} \quad (35)$$

where the modified residuals and tangent matrices are given as

$$\mathbf{k}_{dd}^* = \mathbf{k}_{dd} - \mathbf{k}_{d\boldsymbol{\varsigma}} \mathbf{k}_{\boldsymbol{\varsigma}\boldsymbol{\varsigma}}^{-1} \mathbf{k}_{\boldsymbol{\varsigma}d}, \quad \mathbf{k}_{d\bar{\mathbf{d}}}^* = \mathbf{k}_{d\bar{\mathbf{d}}} - \mathbf{k}_{d\boldsymbol{\varsigma}} \mathbf{k}_{\boldsymbol{\varsigma}\boldsymbol{\varsigma}}^{-1} \mathbf{k}_{\boldsymbol{\varsigma}\bar{\mathbf{d}}}, \quad (36)$$

$$\mathbf{k}_{\bar{\mathbf{d}}d}^* = \mathbf{k}_{\bar{\mathbf{d}}d} - \mathbf{k}_{\bar{\mathbf{d}}\boldsymbol{\varsigma}} \mathbf{k}_{\boldsymbol{\varsigma}\boldsymbol{\varsigma}}^{-1} \mathbf{k}_{\boldsymbol{\varsigma}d}, \quad \mathbf{k}_{\bar{\mathbf{d}}\bar{\mathbf{d}}}^* = \mathbf{k}_{\bar{\mathbf{d}}\bar{\mathbf{d}}} - \mathbf{k}_{\bar{\mathbf{d}}\boldsymbol{\varsigma}} \mathbf{k}_{\boldsymbol{\varsigma}\boldsymbol{\varsigma}}^{-1} \mathbf{k}_{\boldsymbol{\varsigma}\bar{\mathbf{d}}}, \quad (37)$$

$$\mathbf{R}_{\text{int}}^{d*} = \mathbf{R}_{\text{int}}^d - \mathbf{k}_{d\boldsymbol{\varsigma}} \mathbf{k}_{\boldsymbol{\varsigma}\boldsymbol{\varsigma}}^{-1} \mathbf{R}_{\text{int}}^\varsigma, \quad \mathbf{R}_{\text{int}}^{\vartheta*} = \mathbf{R}_{\text{int}}^\vartheta - \mathbf{k}_{\bar{\mathbf{d}}\boldsymbol{\varsigma}} \mathbf{k}_{\boldsymbol{\varsigma}\boldsymbol{\varsigma}}^{-1} \mathbf{R}_{\text{int}}^\varsigma. \quad (38)$$

#### 4.2.3 Interpolation of the enhancing strains

In the following, we briefly address the design of the interpolation operator associated with enhancing modes in order to alleviate Poisson thickness and volumetric locking issues. It is worth mentioning that alternative shell formulations have been proposed to alleviate the Poisson thickness locking issues, such as the quadratic interpolation of the normal displacements to the shell [24], or reduced integration formulations with stabilization techniques for the avoidance of volumetric locking [57, 58].

One of the possible choices that leads to pass the membrane and out-of-plane bending tests along with the avoidance of volumetric (for near incompressible analysis) and Poisson thickness locking consists of

the seven enhancing modes proposed by Vu Quoc and Tan [55], see the comprehensive analysis with regard to the different enhancing schemes examined in [60]. Following this strategy, the interpolation matrix of the enhancing modes via the local operator  $\tilde{\mathbf{M}}(\boldsymbol{\xi})$ , which is defined in the element parametric space, takes the form:

$$\tilde{\mathbf{M}}(\boldsymbol{\xi}) = \begin{bmatrix} \xi^1 & 0 & 0 & 0 & 0 & 0 & 0 \\ 0 & \xi^2 & 0 & 0 & 0 & 0 & 0 \\ 0 & 0 & \xi^3 & \xi^1 \xi^3 & \xi^2 \xi^3 & 0 & 0 \\ 0 & 0 & 0 & 0 & 0 & \xi^1 & \xi^2 \\ 0 & 0 & 0 & 0 & 0 & 0 & 0 \\ 0 & 0 & 0 & 0 & 0 & 0 & 0 \end{bmatrix}. \quad (39)$$

In applications dealing with compressible materials, the number of enhancing parameters can be reduced from 7, Eq.(39), to 3. In such cases, the particular form of the matrix  $\tilde{\mathbf{M}}(\boldsymbol{\xi})$  becomes

$$\tilde{\mathbf{M}}(\boldsymbol{\xi}) = \begin{bmatrix} 0 & 0 & 0 \\ 0 & 0 & 0 \\ \xi^3 & \xi^1 \xi^3 & \xi^2 \xi^3 \\ 0 & 0 & 0 \\ 0 & 0 & 0 \\ 0 & 0 & 0 \end{bmatrix}. \quad (40)$$

Analyzing the previous enhancing scheme, it can be observed that the numerical efforts can be significantly reduced. This has a direct consequence on the numerical efficiency of the proposed formulation.

Finally, in order to fulfill the orthogonality constrain with respect to the stress field and to comply with the so-called patch test, the operator  $\mathbf{M}(\boldsymbol{\xi})$  introduced in Eq.(22) can be computed as follows [66]:

$$\tilde{\mathbf{E}} = \left[ \frac{\det \mathbf{J}_0}{\det \mathbf{J}} \right] \mathbf{T}_0 \tilde{\mathbf{M}}(\boldsymbol{\xi}) \boldsymbol{\varsigma} = \mathbf{M}(\boldsymbol{\xi}) \boldsymbol{\varsigma}, \quad (41)$$

where  $\mathbf{J} = [\mathbf{G}_1, \mathbf{G}_2, \mathbf{G}_3]$ ,  $\mathbf{J}_0 = [\mathbf{G}_{1(0)}, \mathbf{G}_{2(0)}, \mathbf{G}_{3(0)}]$  identify the Jacobian and its evaluation at the element center, and the components of the transformation matrix  $\mathbf{T}$  are given as:  $T^{ij} = \mathbf{G}^i \cdot \mathbf{G}_{(0)}^j$ . The definition of the projection matrix  $\mathbf{T}_0$  is identical to that expressed in [66].

#### 4.2.4 The ANS method

In this section, we succinctly discuss the assumed strain interpolation with regard to the transverse shear ( $E_{13}$  and  $E_{23}$ ) and the transverse thickness ( $E_{33}$ ) strain components based on the ANS method [53]. The combination of the EAS and ANS methods have been profusely adopted in different shells and solid shell formulations, see [47] and the references therein.

The chosen assumed strain interpolations in the current strategy follow the guidelines proposed by Dvorkin and Bathe [53] for the treatment of the transverse shear components ( $E_{13}$  and  $E_{23}$ ), and that developed by Betsch and Stein [54] to modify transverse normal strain components ( $E_{33}$ ), respectively.

The collocation points for the treatment of the transverse shear components are:  $\boldsymbol{\xi}_A = \{\boldsymbol{\xi}_{A_1}, \boldsymbol{\xi}_{A_2}\} = \{(0, -1, 0), (0, 1, 0)\}$  and  $\boldsymbol{\xi}_B = \{\boldsymbol{\xi}_{B_1}, \boldsymbol{\xi}_{B_2}\} = \{(-1, 0, 0), (1, 0, 0)\}$ , see Fig. 3. Thus, the assumed interpolation scheme for the transverse shear strain components  $E_{13}$  and  $E_{23}$  can be expressed as

$$E_{13}^{ANS} = \sum_{i=1}^2 (1 + \xi_{A_i}^2 \xi^2) E_{13}(\boldsymbol{\xi}_A) \quad \text{and} \quad E_{23}^{ANS} = \sum_{i=1}^2 (1 + \xi_{B_i}^1 \xi^1) E_{23}(\boldsymbol{\xi}_B). \quad (42)$$

Similarly, for the treatment of the trapezoidal locking, the coordinates of the chosen collocation points are:  $\boldsymbol{\xi}_C = \{\boldsymbol{\xi}_{C_1}, \boldsymbol{\xi}_{C_2}, \boldsymbol{\xi}_{C_3}, \boldsymbol{\xi}_{C_4}\} = \{(-1, -1, 0), (-1, 1, 0), (1, 1, 0), (1, -1, 0)\}$ , see Fig. 3. Consequently, the assumed interpolation of the component  $E_{33}$  can be computed as:

$$E_{33}^{ANS} = \sum_{i=1}^4 \frac{1}{4} (1 + \xi_{C_i}^1 \xi^1) (1 + \xi_{C_i}^2 \xi^2) E_{33}(\boldsymbol{\xi}_C). \quad (43)$$

Note that the current procedure requires the consistent modification of the corresponding entries of the B-operator, and consequently the associated terms of the geometrical stiffness matrix.

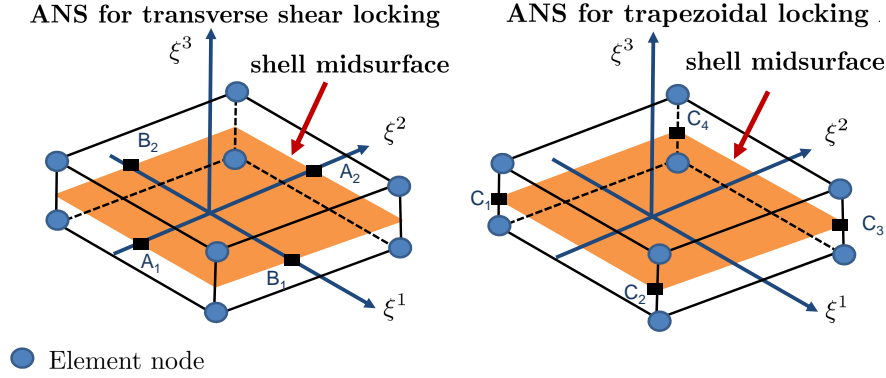


Fig. 3: Definition of the collocation points in the element parametric space for the alleviation of the transverse shear and trapezoidal locking through the ANS method.

## 5 Constitutive formulation and numerical implementation

### 5.1 Constitutive models

The current study is focused on the use of standard isotropic material models. The first model herein considered is the isotropic Kirchhoff-Saint-Venant constitutive formulation, which is characterized by the Young's modulus  $E$  and the Poisson's ratio  $\nu$ . This material law is valid for large displacements but small strains. Based on the standard arguments [59], the tangent material tensor can be formally obtained as:  $\mathbb{C} = \partial_{\mathbf{E}\mathbf{E}}\Psi(\mathbf{E})$ . Its particular form in the convective curvilinear setting is given as

$$\mathbb{C} = [\lambda G^{ij} G^{kl} + \mu (G^{ik} G^{jl} + G^{il} G^{jk})] \mathbf{G}_i \otimes \mathbf{G}_j \otimes \mathbf{G}_k \otimes \mathbf{G}_l, \quad (44)$$

where  $\lambda$  and  $\mu$  denote the Lamé constants.

The second formulation under consideration is the compressible Neo-Hookean material model in the form adopted in [61] in terms of the right Cauchy-Green strain tensor. The corresponding free-energy function, the second Piola-Kirchhoff stress tensor and the tangent material operator are given as

$$\Psi(\mathbf{C}) = \frac{\lambda}{2} (\ln J)^2 - \mu \ln J + \frac{\mu}{2} (\text{tr}[\mathbf{C}] - 3), \quad (45a)$$

$$\mathbf{S}(\mathbf{C}) = 2\partial_{\mathbf{C}}\Psi(\mathbf{C}) = (\lambda \ln J - \mu) \mathbf{C}^{-1} + \mu \mathbb{I}_2, \quad (45b)$$

$$\mathbb{C}(\mathbf{C}) = 4\partial_{\mathbf{C}\mathbf{C}}\Psi(\mathbf{C}) = \lambda \mathbf{C}^{-1} \otimes \mathbf{C}^{-1} + 2(\lambda \ln J - \mu) \frac{\partial \mathbf{C}^{-1}}{\partial \mathbf{C}}, \quad (45c)$$

where  $J$  denotes the determinant of the deformation gradient  $\mathbf{F}$  and  $\text{tr}[\bullet]$  identifies the trace of the tensor  $\bullet$ . Note that the computation of  $J$  requires the consideration of the incompatible strains. In this context, the adoption of the additive decomposition of the Green-Lagrange strain tensor outlined above due to the EAS method (Section 4.1) requires the computation of the modified right Cauchy-Green tensor [57]. Since the displacement derived right Cauchy-Green tensor ( $\mathbf{C}^u$ ) can be obtained only in terms of deformation  $\mathbf{F}^u$  ( $\mathbf{C}^u := (\mathbf{F}^u)^T \mathbf{F}^u$ ), the examination of the corresponding definition can be exploited in order to compute the enhanced right Cauchy-Green tensor  $\mathbf{C}$  as follows:

$$\mathbf{C} := \mathbf{C}^u + \tilde{\mathbf{C}} = 2(\mathbf{E}^u + \tilde{\mathbf{E}}) + \mathbb{I}_2. \quad (46)$$

Note that  $\tilde{\mathbf{C}}$  specifically accounts for the metrics modification due to the EAS method [1]. Moreover, for constitutive formulations defined in terms of the deformation gradient, Hauptmann and coauthors [57] proposed a procedure rooted in the polar decomposition ( $\mathbf{F} = \mathbf{R}\mathbf{U}$ , where  $\mathbf{R}$  is the rotation tensor, and  $\mathbf{U}^2 = 2\mathbf{E} + \mathbb{I}_2$  stands for the modified right-stretch tensor), which leads to the computation of the modified deformation gradient  $\mathbf{F}$ .

## 5.2 Implementation aspects: numerical treatment of the EAS method

The current solid shell formulation is implemented into the FE packages ABAQUS and FEAP [62] by means of user-defined capabilities. With regard to the visualization of the computed results, the package **Paraview** is used to process the FEAP output, while the ABAQUS version employs overlapped elements with very low stiffness properties, see [63].

The algorithmic treatment of the EAS method in nonlinear computations requires a special attention due to the fact that the update of the internal parameters  $\varsigma$  along the loading procedure is required. Alternatively to the computational procedures discussed in Simo et al. [64], in which the authors proposed an iterative local Newton-Raphson scheme at the element level to perform the required update, we used a modified version of the approach addressed in [63]. An outline of the computational procedure is drafted in Algorithm 1. In particular, this process employs information corresponding to the previous converged state, making use of the so-called history variables that most of the FE codes offer, i.e. **hr** and **svars** vectors within FEAP and ABAQUS, respectively. This strategy comprises several advantages especially in terms of its relative simplicity to be implemented and the significant savings regarding the data storage at the element level, among other aspects.

This methodology is detailed as follows. Within the time increment  $[t_n, t_{n+1}^{(k)}]$  along the solution procedure (denoting  $\Delta\tau = t_{n+1}^{(k)} - t_n$ ), where  $t_n$  and  $t_{n+1}^{(k)}$  identify the previous converged state and the prospective current time step at the global iteration  $k$ , respectively, given the initial data  $\{\mathbf{d}_n, \varsigma_n, \bar{\mathfrak{d}}_n\}$  (with  $\varsigma_n$  being stored as internal variables), the nonlinear solution procedure requires the iteration around the intermediate state  $\{\mathbf{d}_{n+1}^{(k)}, \varsigma_{n+1}^{(k)}, \bar{\mathfrak{d}}_{n+1}^{(k)}\}$  to achieve the final solution at  $t_{n+1}^{(k)}$ . We introduce the following notation:  $\mathbf{d}_n, \varsigma_n$  and  $\bar{\mathfrak{d}}_n$  identify the element-wise variables at the previously converged state  $t_n$ , whereas  $\mathbf{d}_{n+1}^{(k)}, \varsigma_{n+1}^{(k)}$  and  $\bar{\mathfrak{d}}_{n+1}^{(k)}$  denote the element kinematic field, the phase field and incompatible strain field on the element level at the tentative current time step  $n + 1$  at the iteration  $k$ , respectively. Due to the exploitation of the static condensation procedure (Section 4.2.2), the nodal displacements and phase field variables are defined as primary unknowns at the element level, and therefore the increment of the incompatible strains at the current time step  $\Delta\varsigma_n^{(k)}$  should be accordingly determined. Recalling the process described in [63], through the third row of Eq.(33), the increment of the enhancing strains at a given iteration  $k$  within the time increment  $[t_n, t_{n+1}^{(k)}]$  can be computed as:

$$\Delta\varsigma_n^{(k)} = -[\mathbf{k}_{\varsigma\varsigma, n}]^{-1} \left[ \mathbf{R}_{\text{int}, n}^{\varsigma} + \mathbf{k}_{\varsigma d, n} \Delta\mathbf{d}^{(k)} + \mathbf{k}_{\varsigma \bar{\mathfrak{d}}, n} \Delta\bar{\mathfrak{d}}^{(k)} \right]. \quad (47)$$

The incremental magnitudes  $\Delta\mathbf{d}^{(k)}$  and  $\Delta\bar{\mathfrak{d}}^{(k)}$  are usually provided by the numerical solver since they correspond to the nodal degrees of freedom, whereas the element matrices at the state  $t_n$  in Eq.(47) can be obtained by the simple computation of the previous converged solution as follows:  $t_n = t_{n+1}^{(k)} - \Delta\tau^{(k)}$ , so that  $\mathbf{d}_n = \mathbf{d}_{n+1}^{(k)} - \Delta\mathbf{d}^{(k)}$  and  $\bar{\mathfrak{d}}_n = \bar{\mathfrak{d}}_{n+1}^{(k)} - \Delta\bar{\mathfrak{d}}^{(k)}$ .

Note that the update procedure expressed in Eq.(47) can be notably simplified in the case of staggered (sequential) solution schemes, due to the fact that the phase field is not affecting the EAS operators.

In addition to the previous considerations, as discussed in [63], the proposed numerical procedure requires the inversion of the elemental matrix  $\mathbf{k}_{\varsigma\varsigma}$  at the time  $t_n$  and  $t_{n+1}$ . This matrix depends on the number of EAS-modes consider to prevent locking (7 in the present investigation, which can be reduced to 3 internal variables if only the Poisson thickness locking is alleviated), so that the computational efforts to carry out such inversions penalize the efficiency of this strategy.

Finally, since the element stiffness is degraded using the function  $\mathfrak{g}(\bar{\mathfrak{d}})$  as damage progresses, this issue can lead to numerical problems for the computation of  $[\mathbf{k}_{\varsigma\varsigma}]^{-1}$  for values of  $\bar{\mathfrak{d}}$  relatively close to 1 (fully damage state). In order to preclude this issue, in the current formulation, we consider that the coupling between the EAS method with the displacements and the phase field is neglected when the average value of  $\bar{\mathfrak{d}}$  at the element level is higher than 0.75. Nevertheless, the robustness and simplicity of the procedure for every kind of multi-field nonlinear FE applications is noteworthy.

## 6 Numerical examples

In this section, the simulation capabilities of the proposed phase field modeling for mixed shell formulations are examined by means of several numerical examples. We focus our analysis on small and large

- Data:** Given  $\{\mathbf{d}_n, \boldsymbol{\varsigma}_n, \bar{\mathbf{d}}_n, \}$  that correspond to the data at time  $t_n$ , the history variables  $\boldsymbol{\varsigma}_n$ , and the projective nodal solution  $\{\mathbf{d}_{n+1}^{(k)}, \bar{\mathbf{d}}_{n+1}^{(k)}\}$  at time  $t_{n+1}^{(k)}$  within the interval  $[t_n, t_{n+1}^{(k)}]$
1. Compute  $\Delta \mathbf{d} = \mathbf{d}_{n+1}^{(k)} - \mathbf{d}_n$  and  $\Delta \bar{\mathbf{d}}^{(k)} = \bar{\mathbf{d}}_{n+1}^{(k)} - \bar{\mathbf{d}}_n$ ;
  2. Loop over the integration points based on the previous converged configuration  $t_n$ ;
    - 2.1 Compute the curvilinear basis  $\mathbf{G}_n$  and  $\mathbf{g}_n$ ;
    - 2.2 Compute the B-operator  $\mathbf{B}_n$ ;
    - 2.3 Modify the B-operator due to ANS method Eqs.(42)-(43);
    - 2.4 Compute the constitutive matrix  $\mathbb{C}_n$  and stress tensors  $\mathbf{S}_n$ ;
    - 2.5 Interpolate the nodal phase field values;
    - 2.6 Compute the EAS-operator  $\mathbf{M}_n$ ;
  3. Compute the matrices:  $\mathbf{k}_{\varsigma d, n}$ ,  $\mathbf{k}_{\varsigma \bar{d}, n}$  and  $\mathbf{k}_{\varsigma \varsigma, n}$  and the internal force vector  $\mathbf{R}_{\text{int}, n}^{\varsigma}$ ;
  4. Compute Eq.(47):  $\Delta \boldsymbol{\varsigma}_n^{(k)} = -[\mathbf{k}_{\varsigma \varsigma, n}]^{-1} [\mathbf{R}_{\text{int}, n}^{\varsigma} + \mathbf{k}_{\varsigma d, n} \Delta \mathbf{d}^{(k)} + \mathbf{k}_{\varsigma \bar{d}, n} \Delta \bar{\mathbf{d}}^{(k)}]$ ;
  5. Update the enhancing parameters:  $\boldsymbol{\varsigma}_{n+1}^{(k)} = \boldsymbol{\varsigma}_n + \Delta \boldsymbol{\varsigma}_n^{(k)}$ ;
  6. Loop over the integration points at the current tentative time step  $t_{n+1}^{(k)}$ ;
    - 6.1 Compute the curvilinear basis  $\mathbf{G}_{n+1}^{(k)}$  and  $\mathbf{g}_{n+1}^{(k)}$ ;
    - 6.2 Compute the B-operator  $\mathbf{B}_{n+1}^{(k)}$ ;
    - 6.3 Modify the B-operator due to ANS method (42)-(43);
    - 6.4 Compute the constitutive matrix  $\mathbb{C}_{n+1}^{(k)}$ , stress tensors  $\mathbf{S}_{n+1}^{(k)}$  and the intact free energy  $\Psi_{n+1}^{(k)}$ ;
    - 6.5 Interpolate the nodal phase field values;
    - 6.6 Compute the EAS-operator  $\mathbf{M}_{n+1}^{(k)}$ ;
    - 6.7 Compute the phase field operators  $\mathbf{B}_{n+1}^{\bar{d}(k)}$ ;
    - 6.8 Compute the geometrical stiffness matrix and modify due to ANS method;
  7. Construct the element matrices and the internal force vectors of the complete system Eq.(33);
  8. Compute the static condensation of the EAS variables, Eqs.(35)–(38);
  9. Perform the final assembly;

**Algorithm 1:** Algorithmic treatment of the coupled EAS-phase field modeling based on the previous converged configuration at the pseudo time step  $t_n$ .

strain analysis with the aim of emphasizing the applicability of the current framework for two different types of material constitutive laws.

### 6.1 Plate under tensile loading: assessment of the solution schemes

The first example under consideration investigates the performance of the monolithic and the staggered solution schemes. It is worth mentioning that the current staggered strategy replicates that proposed in [31] and regards the uncoupling between the phase field and the rest of the independent fields at the element level, i.e. the displacements and the enhanced strains.

In particular, we consider a squared plate of side length equal to 20 mm which is subjected to uniform in-plane tensile loading. Therefore, only membrane stress states are developed. An imposed displacement  $\Delta$  is set to all points of the top edge of the plate, whereas the points of the opposite edge are fully restrained. The material properties are:  $E = 2 \times 10^{11} \text{ N/m}^2$ ,  $\nu = 0$ ,  $\mathcal{G}_c = 2 \text{ N/m}$  and  $l = 0.05 \text{ mm}$ . Note that, since no initial notch is considered, damage evolves in the whole domain of the plate.

The total force of the system, computed as the sum of the reaction forces acting on the restrained side of the plate, is plotted vs. the imposed displacement in Fig. 4, for the proposed monolithic and for the staggered solution schemes. The proposed monolithic approach, with a pseudo-time step increment  $\Delta \tau = 0.01$  is providing a very smooth mechanical response, both in the pre-peak branch and in the softening regime, as highlighted in the magnified portion of the plot in Fig. 4. The staggered solution scheme, on the other hand, presents a series of small oscillations whose amplitude diminishes by reducing the pseudo-time step increment.

Regarding the convergence properties (Fig. 5), whereas the monolithic approach displays a quadratic convergence, the staggered solution scheme presents a slightly worse performance for a generic time step. The error in the residual norm of the staggered solution scheme can be reduced and eventually converges to that corresponding to the monolithic approach by reducing the pseudo-time step increment.

Finally, with reference to the overall computation time, the monolithic and the staggered schemes have almost the same performance for a given pseudo-time step increment. However, in order to reduce

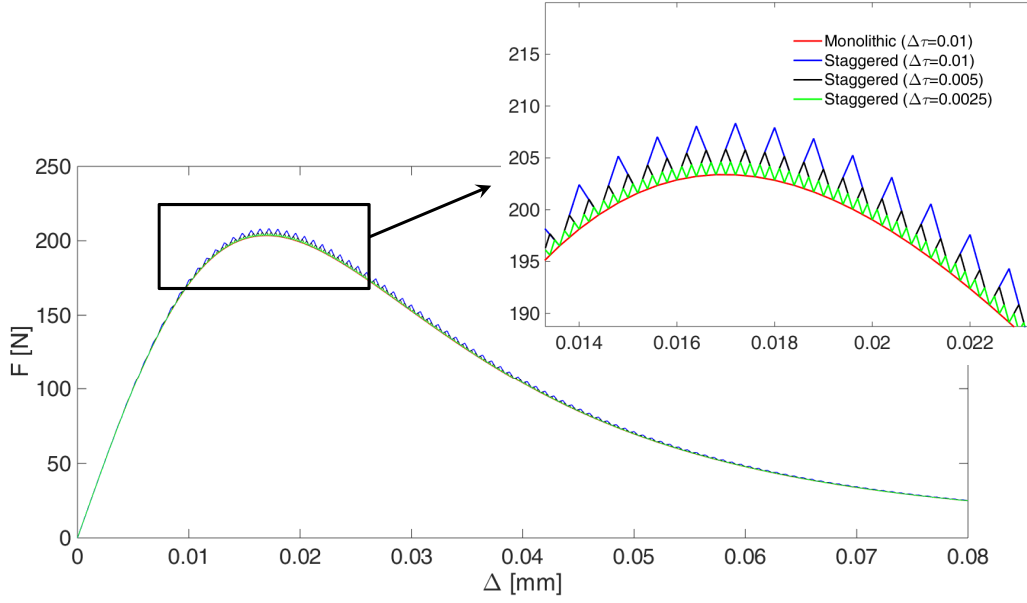


Fig. 4: Total force vs. imposed displacement curve for the uniaxial test problem. The performance of the monolithic scheme is compared with that of the staggered approach, for different pseudo-time step increments.

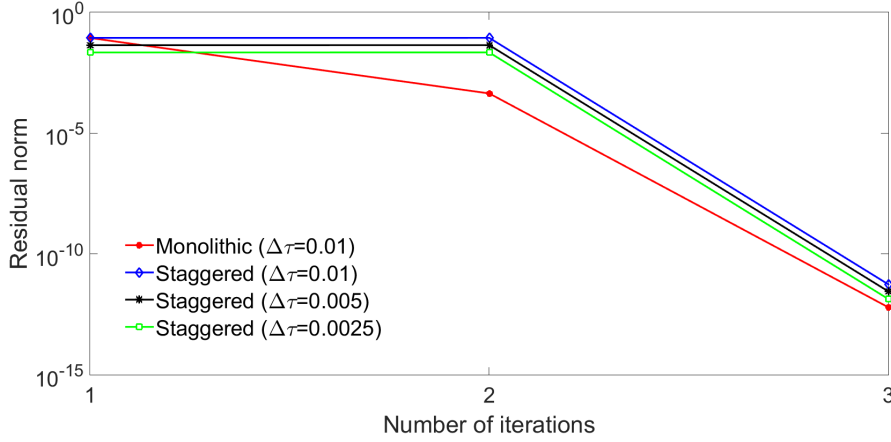


Fig. 5: Convergence properties of the monolithic and staggered solution schemes, for different pseudo-time step increments. Note the convergence of the staggered scheme to the monolithic approach by refining the pseudo-time step increment  $\Delta\tau$ .

the amount of [oscillations](#) observed in the staggered solution (see Fig. 4), a reduction of the pseudo-time step increment from 0.01 to 0.005 and then to 0.0025 is required. This fact leads to a significant increase in the CPU time, see Fig. 6.

## 6.2 In-plane fracture tension tests

The first test herein proposed is the benchmark problem previously considered by Miehe and coauthors [30] for 2D fracture simulations, which has been subsequently re-examined in [44] for testing phase field fracture in a solid shell based on an isogeometric discretization. The geometry of the test problem is a

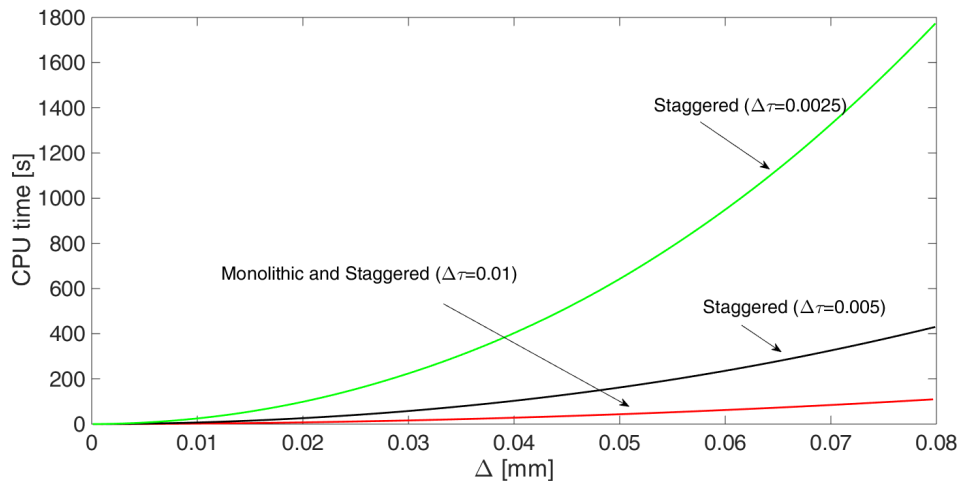


Fig. 6: CPU time of the monolithic and staggered solution schemes, for different pseudo-time step increments. Although the two approaches require almost the same CPU time for a given pseudo-time step increment, a finer time step increment should be used in the staggered scheme to achieve a smoother mechanical response as in the monolithic approach, which leads to a significant increase in CPU time..

squared plate of unit lateral size  $2L = 1$  mm and thickness  $t = 0.1$  mm, with an initial sharp notch of length  $L$  placed in the middle of the plate, see Fig. 7. The lower side of the plate is restrained towards the vertical direction, while uniform vertical displacements are applied to the opposite side. This loading condition is leading to a symmetric stress field at the notch tip, promoting Mode I crack propagation. The plate is discretized using 15000 elements with localized refinements around the region of the potential crack development.

The first case comprises the Kirchhoff-Saint-Venant material law, with Lamé constants:  $\lambda = 121.15 \times 10^3$  N/mm<sup>2</sup>,  $\mu = 80.77 \times 10^3$  N/mm<sup>2</sup>. The phase field parameters are set:  $\mathcal{G}_c = 2.7$  N/mm and  $l = 0.015$  mm. The simulation is performed under displacement control using a fixed displacement increment.

The contour plot of the phase field variable of the FEAP version of the current formulation, superimposed to the deformed shape of the plate magnified by a factor 20, is shown in Fig. 8 for three different deformation levels. The resulting crack path is consisting with those previously reported in [30,31,42]. The previous analysis is also conducted considering the Neo-Hookean constitutive relation, activating geometric nonlinear effects and including both the ANS and the EAS locking remedies. Fig. 9 shows the load-displacement evolution curve of the current application for Kirchhoff-Saint-Venant and Neo-Hookean material formulations. In this graph, it can be observed that the evolution corresponding to the nonlinear material formulation is characterized by a slightly higher maximum load and a less pronounced decay in the post-peak evolution in comparison to the linear constitutive model. Note also that the predicted fracture path is independent of the material formulation, see Fig. 9 for the crack pattern obtained in output from ABAQUS.

In line with the analysis performed in [60], we examine the eigenvalues of the current solid shell for nearly incompressible limit. Differing from other locking pathologies, volumetric locking cannot be avoided by means of mesh refinement due to the fact that some normal strain components are missing. For this check, the following mechanical properties are chosen: elastic modulus  $E = 1$  N/mm<sup>2</sup>, Poisson's ratio  $\nu = 0.4999$ . Table 1 reports the high eigenvalues corresponding to the element deformation modes for the pure displacement formulation (SSQ1) and activating the EAS and ANS techniques (SSEAS7ANS). Since the element stiffness matrix should contain only one eigenvalue that tends to infinity (corresponding to the dilatation mode), the current fully integrated solid shell satisfies this condition when the EAS and ANS methods are activated according to the interpolation scheme detailed in Eq.(39). Fig. 10 depicts the load-displacement evolution curve corresponding to the current in-plane fracture application for a nearly incompressible Kirchhoff-Saint-Venant material model using the same discretization and with a staggered solution scheme with  $\Delta\tau = 0.01$ . In this graph, as was discussed above, small oscillations along the evolution can be observed, especially when the crack is developed, but nevertheless these results are

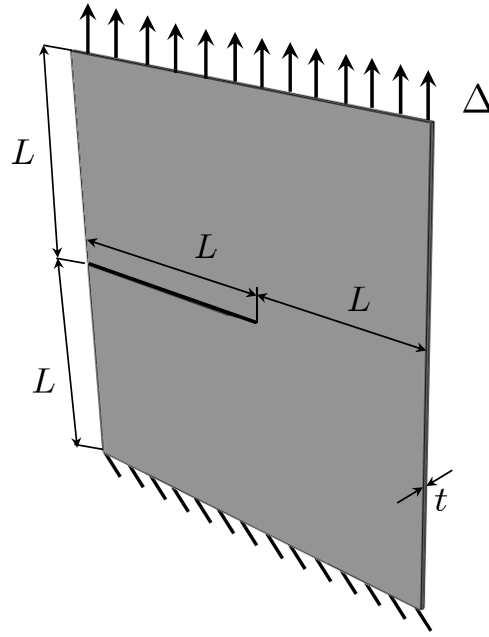


Fig. 7: In-plane tensile fracture test: geometry and boundary conditions.

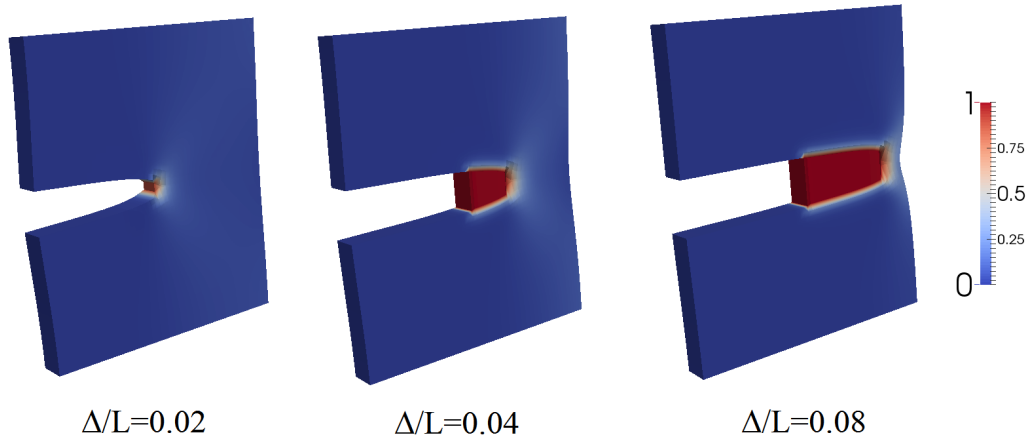


Fig. 8: In-plane tensile fracture test: contour plots of the phase field variable superimposed to the deformed shape of the plate, with an amplification factor 20, for three different values of the dimensionless imposed displacement  $\Delta$  to top side of the plate. The variable  $L$  denotes the lateral mid-size of the square plate.

in good overall agreement with the monolithic version. In addition, note that from the qualitative point of view, higher values for the maximum reaction force and the imposed displacement are required to achieve the complete separation of the plate into two parts in comparison with the compressible case, see Fig. 9.

The second in-plane test consists of the same square plate with the straight horizontal notch, replicating the previous mechanical and fracture properties subjected to in-plane shear loading mode. The applied boundary conditions are (Fig. 11.a): (i) a horizontal displacement is applied to the top edges of the plate, and (ii) fully restrained displacements at the bottom edges of the plate. Focusing on geometrically linear analysis, we adopt the following positive-negative decomposition of the free energy density

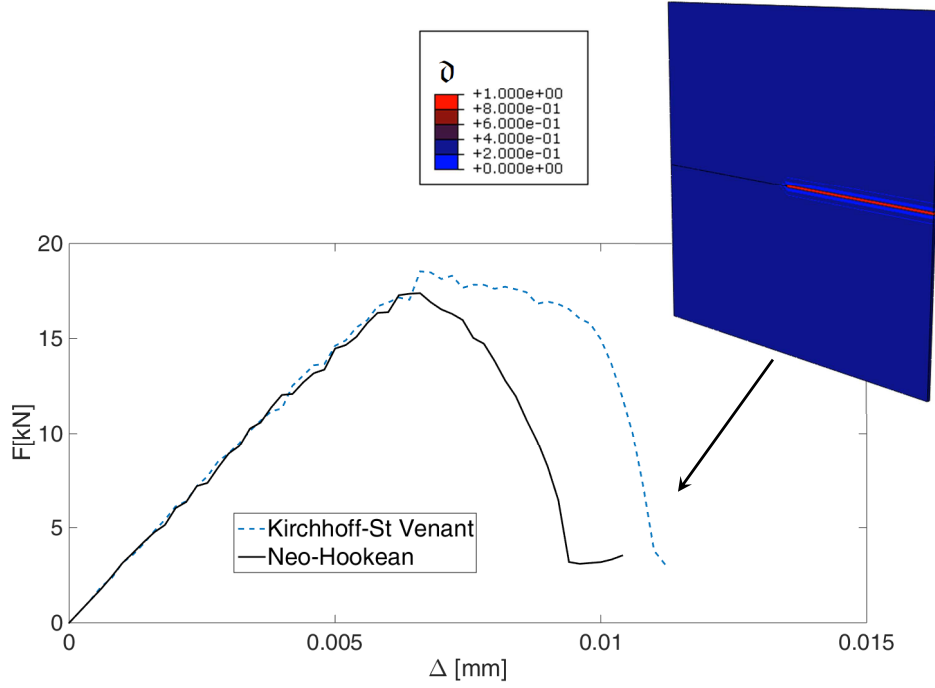


Fig. 9: In-plane tensile fracture test: load-displacement evolution curves for Kirchhoff-Saint-Venant and Neo-Hookean material models.

Mode	SSQ1	SSEAS7ANS
12	92.654	0.333
13	92.654	0.333
14	92.654	0.333
15	555.650	0.333
16	555.650	0.364
17	555.650	0.364
18	2500.000	2500.000

Table 1: Solid shell formulation: (higher) eigenvalues for a unit cube for near incompressibility. SSQ1 denotes the pure displacement solid shell formulation, whereas SSEAS7ANS identifies the proposed solid shell model activating the EAS with 7 enhancing strains, Eq.(39), and the ANS methods.

in the bulk according to [30,31]:

$$\psi(\boldsymbol{\varepsilon}, \mathfrak{d}) = \mathfrak{g}(\mathfrak{d})\psi_+^e(\boldsymbol{\varepsilon}) + \psi_-^e(\boldsymbol{\varepsilon}), \quad (48a)$$

$$\psi_+^e(\boldsymbol{\varepsilon}) = \frac{\lambda}{2} (\langle \text{tr}[\boldsymbol{\varepsilon}] \rangle_+)^2 + \mu \text{tr}[\boldsymbol{\varepsilon}_+^2], \quad (48b)$$

$$\psi_-^e(\boldsymbol{\varepsilon}) = \frac{\lambda}{2} (\langle \text{tr}[\boldsymbol{\varepsilon}] \rangle_-)^2 + \mu \text{tr}[\boldsymbol{\varepsilon}_-^2], \quad (48c)$$

where  $\boldsymbol{\varepsilon}$  stands for the small strain tensor and  $\text{tr}[\bullet]$  identifies the trace operator. In the previous expressions, the decomposition of the strain tensor into its positive and negative counterparts,  $\boldsymbol{\varepsilon} = \boldsymbol{\varepsilon}_+ + \boldsymbol{\varepsilon}_-$ , is recalled to trigger damage only under tensile loading. The spectral decomposition of the positive part of the strain tensor reads  $\boldsymbol{\varepsilon}_+ = \sum_{i=1}^{n_{dim}} \langle \boldsymbol{\varepsilon}^i \rangle_+ \mathbf{n}_\varepsilon^i \otimes \mathbf{n}_\varepsilon^i$ , where  $\boldsymbol{\varepsilon}^i$  and  $\mathbf{n}_\varepsilon^i$  identify the eigenvalues and the eigenvectors of the strain tensor and  $\langle \bullet \rangle_+ = (\bullet + |\bullet|)/2$ . This decomposition leads to slight modifications in the corresponding numerical implementation. The simulations are conducted using the previous finite element mesh under displacement control. Fig. 11.b shows the contour plot of the phase field variable of the FEAP version of current formulation, whose crack paths satisfactorily coincides with those predicted in previous studies [30,31,38,44].

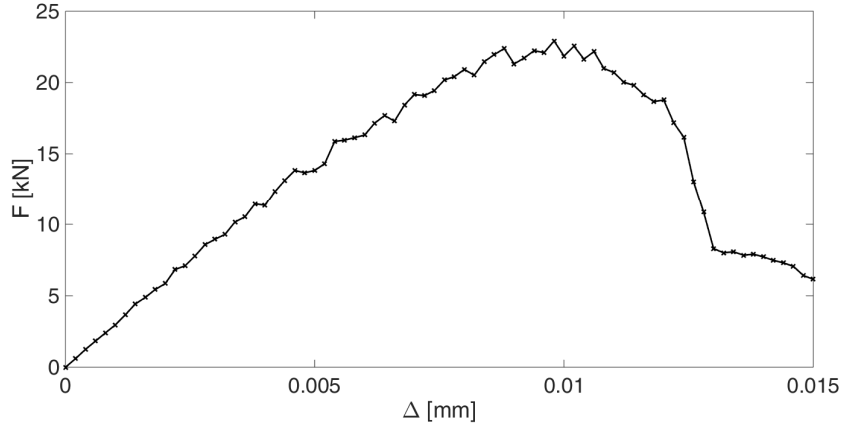


Fig. 10: In-plane tensile fracture test: load-displacement evolution curve for Kirchhoff-Saint-Venant material model for nearly incompressible limit.

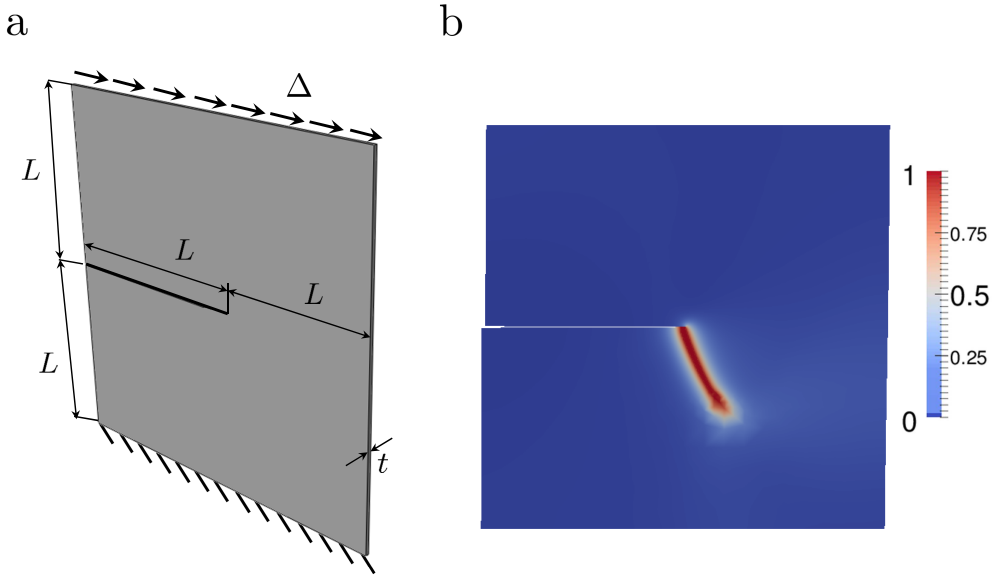


Fig. 11: In-plane shear fracture test. (a) Geometry and boundary conditions. (b) Contour plot of the phase field variable superimposed to the deformed shape of the plate.

### 6.3 Double edge notched specimen in tension: verification example

This example regards the application of the current approach to the double edge notched specimen under tensile loading for rubber at large strains. This application has been thoroughly discussed by Miehe and coauthors [33] for an alternative phase field formulation obtaining very satisfactory agreements with the experimental data reported in [65].

The geometric description of the specimen is shown in Fig. 12, whose dimensions are: axial length  $L = 200$  mm, width  $B = 80$  mm, thickness  $t = 3$  mm. In this investigation we only consider the configuration with an initial notch length  $a = 20$  mm. The specimen is discretized using approximately 35000 solid shell elements with mesh refinement around the potential crack propagation region.

In order to preserve the consistency with the formulation proposed in [33], a minor modification of the free energy function, Eq.(45a), is introduced as

$$\Psi(\mathbf{C}) = \frac{\mu}{2} (\text{tr}[\mathbf{C}] - 3) + \frac{\mu}{\beta} \left[ (\ln J)^{-\beta} - 1 \right], \quad (49)$$

where the shear modulus  $\mu$  is defined by the micro-mechanical Gaussian model, and the parameter  $\beta$  is related to the Poisson ratio via the following expression:  $\beta = 2\nu/(1 - 2\nu)$ . The derivation of the stress tensor and the corresponding constitutive operator from Eq.(49) are computed according to standard tensorial arguments, see [59]. Replicating [33], the mechanical properties are:  $\mu = 0.203 \text{ N/mm}^2$  and  $\nu = 0.45$ . The fracture parameters correspond to:  $\mathcal{G}_c = 2.67 \text{ N/mm}$  and  $l = 1 \text{ mm}$ . The boundary conditions are set as follows: (i) prescribed displacement of  $\Delta = 50 \text{ mm}$  at the upper surface, and (ii) fully restrained displacements to the nodes belonging to the lower surface. The simulations are performed using the ABAQUS version of the current formulation (the FEAP version yields to identical results) under monotonic imposed displacements with 2500 pseudo-time increments including both the EAS and ANS methods for locking treatment.

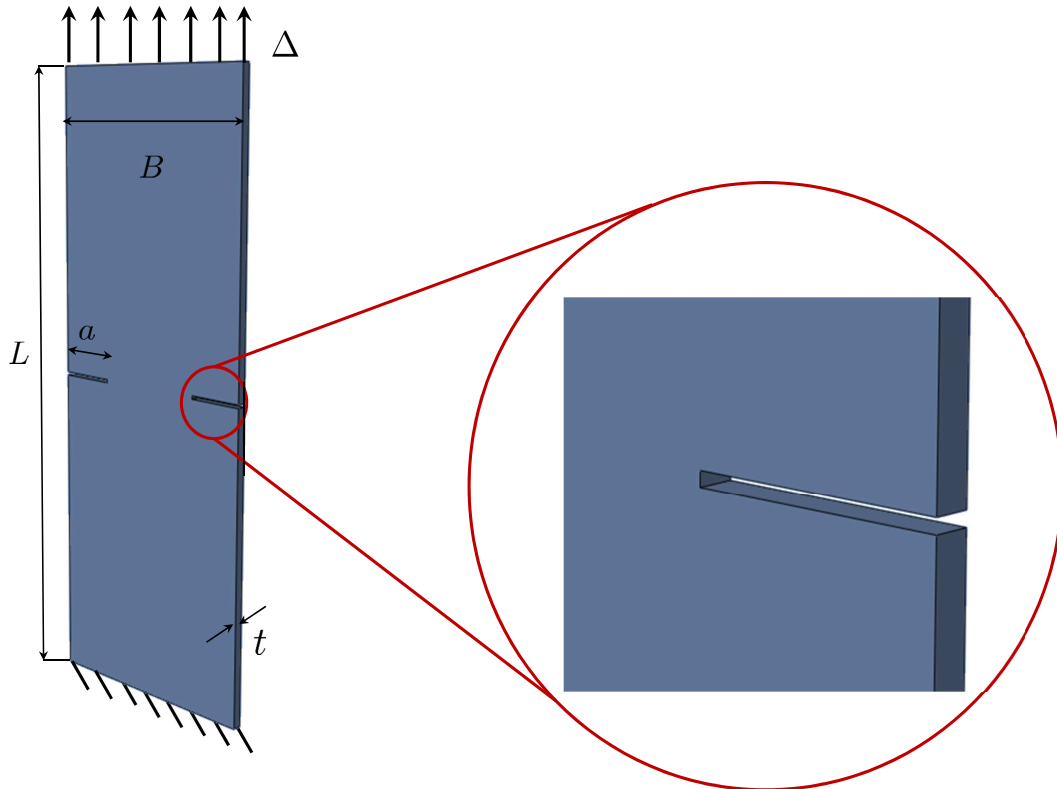


Fig. 12: Double edge notched specimen: geometry and boundary conditions.

Fig. 13 depicts the load-displacement evolution curve of the current simulation and the experimental data [65], where a satisfactory agreement is achieved (also with the outcome of the computations detailed in [33]). In this graph, we observe that nonlinear effects are developed from mid-stages (10-12 kN), which are captured by the current methodology, up to failure. From a qualitative standpoint, the numerical predictions slightly underestimate the experimental peak load (about 25 kN) and the maximum displacement. Note also that a rapid crack evolution is predicted to occur. The corresponding crack pattern is also shown in Fig. 13, being the crack tip concentrated around the notches. These evolutions are in very good agreement with that reported in [33], though in the current simulation the failed elements are not removed from the visualization. These results validate the current approach for thin-walled applications and hyperelastic constitutive models, showing an accurate matching of the experimental data, along with previous predictions based on phase field models.

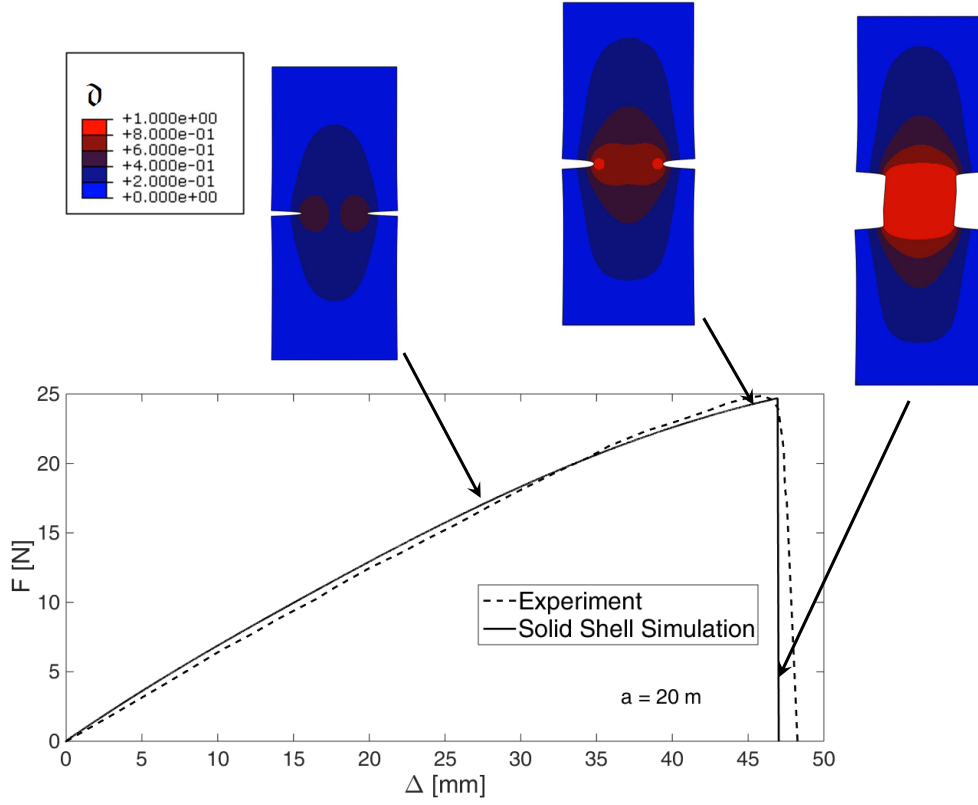


Fig. 13: Double edge notched specimen: experimental-numerical correlation of load-displacement evolution curve and crack patterns at different stages.

#### 6.4 Out-of-plane fracture test

This example concerns the fracture problem of a brittle plate subjected to out-of-plane displacements as shown in Fig. 14. This application includes bending-dominated stress states. The geometric dimensions are: length  $L = 0.3$  mm, width  $B = 0.1$  mm, thickness  $t = 0.01$  mm. A notch of initial length  $a = 0.05$  mm is considered in the middle of the short edge, while the opposite one is fully restrained. Out-of-plane displacements of amplitude  $\Delta = 0.075$  mm are applied in opposite directions to the two half edges separated by the notch in order to promote Mode III crack growth. The plate is made of a Kirchhoff-Saint-Venant material law with Lamé constants:  $\lambda = 121.15 \times 10^3$  N/mm<sup>2</sup> and  $\mu = 80.77 \times 10^3$  N/mm<sup>2</sup>. The critical energy release rate and the length scale parameter for the phase field model are:  $\mathcal{G}_c = 2.7$  N/mm and  $l = 0.002$  mm. The simulation is performed considering geometrical nonlinear effects and including both the ANS and the EAS locking remedies.

The deformed shape of the shell (in scale, without any amplification factor), is shown in Fig. 15 for different values of the imposed displacement  $\Delta$ . The contour plot of the phase field variable is also superimposed to the deformed geometry, showing the evolution of the crack path.

For small values of the imposed displacement, the notch tip is concentrating the phase field variable reaching the cracked state ( $\phi = 1$ ) approximately for  $\Delta = 0.01$  mm. Progressing along the application of the displacement, straight Mode III crack growth takes place, which is then followed by a complex mixed mode propagation, involving, in addition to Mode III, also Mode I and Mode II. Due to this mixed fracture conditions, the crack path deviates from the straight trajectory, leading to two curved paths till the crack tips meet the lateral boundaries of the shell. The increase in the applied displacement leads to a progressive growth of damage around the crack paths as well. The corresponding force-displacement curve in Fig. 16 shows a nonlinear response with decreasing stiffness during the first stage of pure Mode III crack growth, up to  $\Delta = 0.02$  mm, and then a sudden increase in force during the subsequent stage of

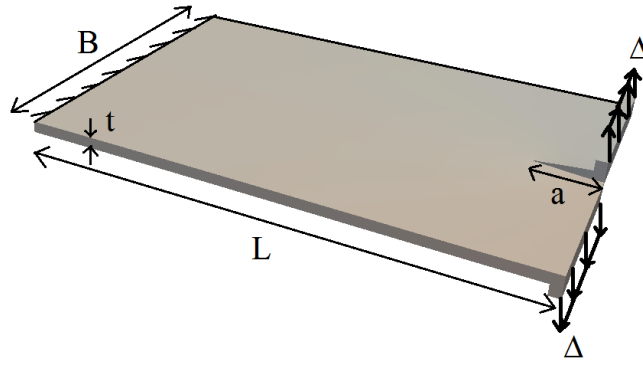


Fig. 14: Sketch of the out-of-plane test problem.

mixed mode crack propagation. For  $\Delta > 0.05$  mm, i.e. when the crack path is almost complete, softening takes place due to the progressive widening of the region subject to nonlocal damage.

This application involves notable bending effects, therefore the variation of the phase field variable over the shell thickness according to the ansatz proposed in Eq.13 can be examined. Fig.17 shows a series of snapshots for the contour plot of the phase field variable around the specimen notch at different stages along the simulation. As can be observed, a variation of the phase field variable over the shell thickness is triggered using the current formulation, see alternative approaches [44, 45, 46].

### 6.5 Fracture of shells with initially curved geometries

Finally, the proposed methodology is examined using an initially curved structure. In particular, we consider a cylindrical shell subjected with a initial through-thickness notch, see Fig. 18. The dimensions of the structure are: length  $L = 340.8$  mm, inner radius  $R = 100.1$  mm, thickness  $t = 3$  mm. The length of the initial notch is set:  $a_0 = \vartheta R$ , with  $\vartheta = \pm 10^\circ$  [44]. The material parameters complying with the Kirchhoff-Saint-Venant constitutive model are: elastic modulus  $E = 2.0685$  N/mm<sup>5</sup>, Poisson's ratio  $\nu = 0.3$ . The fracture parameters replicate those introduced in Section 6.2. Regarding the supporting conditions, right axial edge of the shell is fully clamped, whereas the opposite axial edge is subjected to an uniform displacement  $\Delta$ . The structure is discretized using 2170 elements including a specific refinement in the region where the crack is expected to develop. The simulations are conducted under displacement control with a fixed pseudo-time increment.

Fig. 19 depicts the evolution of the phase field variable at different loading stages. This crack pattern is in close agreement with that discussed in [44], which employed an alternative isogeometric solid shell equipped with phase field capabilities for fracture modeling.

## 7 Concluding remarks

In this work, a novel phase field model of brittle fracture for solid shell relying on a mixed variational principle has been developed and implemented into FE packages. In particular, we exploited the use of the EAS method through the postulation of the multi-field variational principle for the treatment of Poisson thickness and volumetric locking. This numerical technique has been also combined with the ANS method, which is employed for the alleviation of transverse shear and trapezoidal locking effects. The proposed solid shell formulation also included the coupling between the phase field variable with the displacement and the incompatible strain fields.

From the computational standpoint, the main aspects with regard to the treatment of the EAS method in iterative-incremental solution methods and its incorporation into the FE packages FEAP and ABAQUS have been addressed. Special attention has been also devoted to the analysis of monolithic and staggered solution strategies.

The applicability of the proposed model has been demonstrated by means of several applications regarding brittle fracture in hyperelastic bodies, whereby finite strain behavior was coupled with the

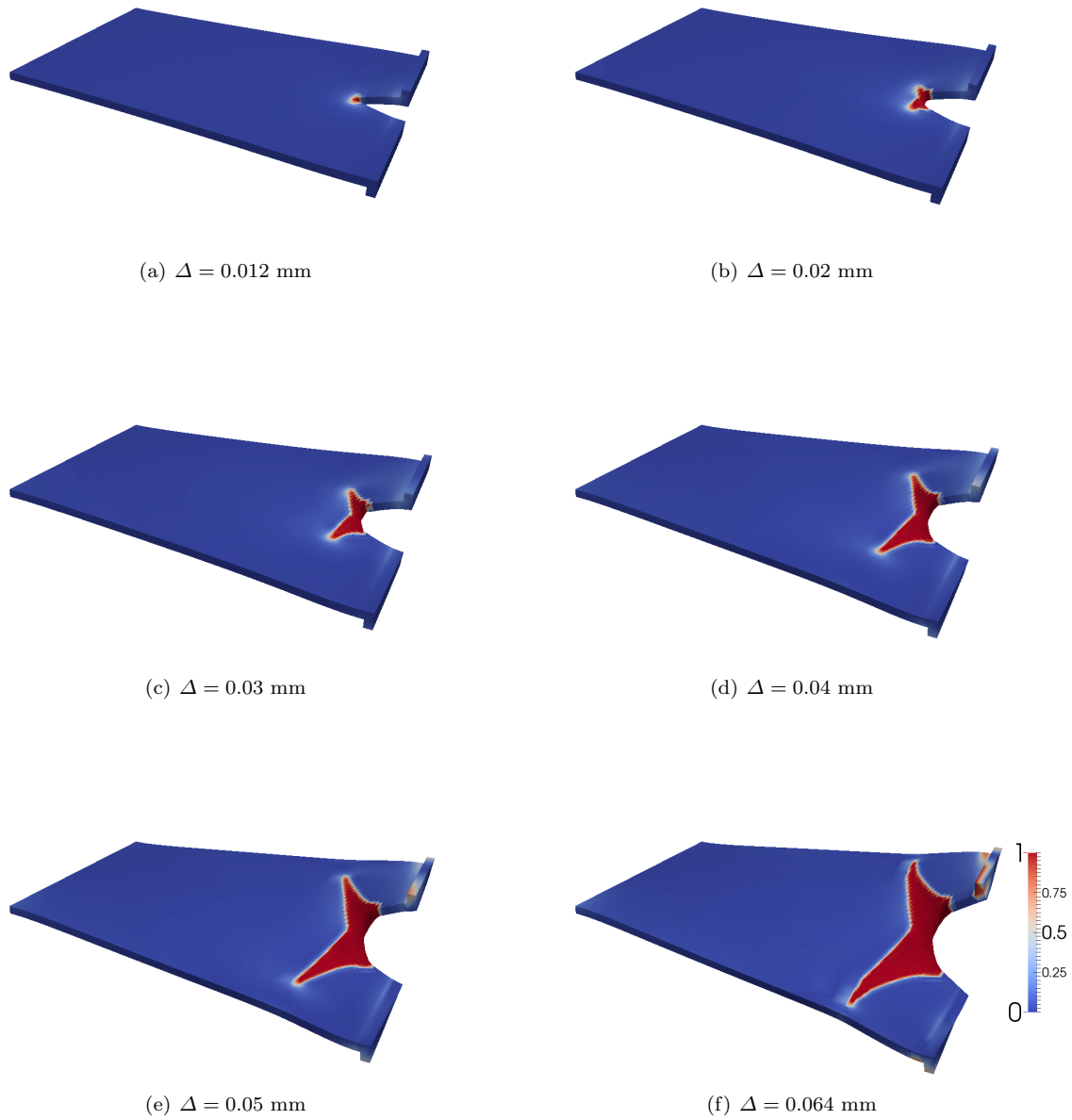


Fig. 15: Out-of-plane test problem: deformed geometry with superimposed contour plot of the phase field variable.

[phase field model](#) using a total Lagrangian formulation. The corresponding results under different loading conditions showed that the proposed modeling strategy is able to capture crack initiation and propagation.

Finally, it is noteworthy that the current formulation can be seen as a potential departure point for alternative mixed FE formulations that can incorporate numerical techniques in order to prevent locking pathologies. Moreover, due to its robustness and versatility, the current solid shell model can be also further extended to account for ductile fracture and multi-physics phenomena in solids.

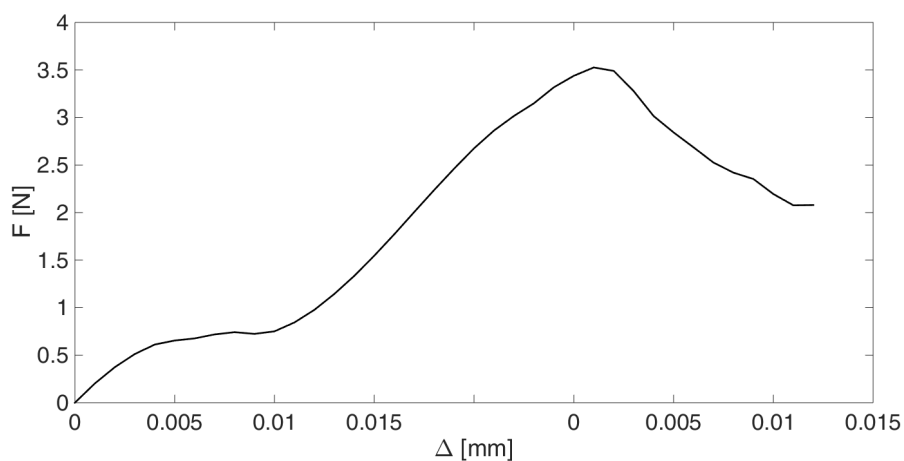


Fig. 16: Out-of-plane test problem: force-displacement curve.

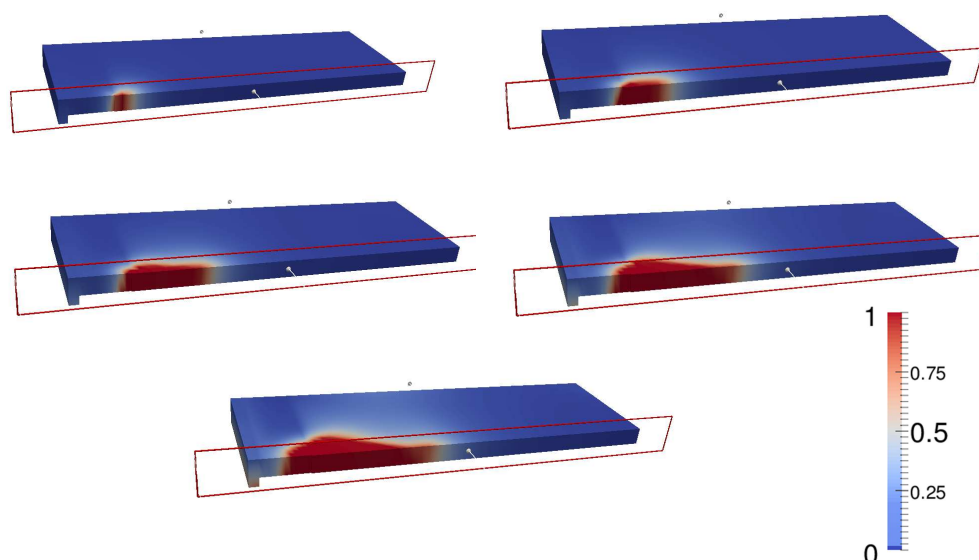


Fig. 17: Out-of-plane test problem: zoom of the contour plot around the specimen notch. Evolution of the phase field variable over the shell thickness at different stages along the simulation.

## Acknowledgements

MP and JR gratefully acknowledge financial support of the European Research Council (ERC), Grant No. 306622 through the ERC Starting Grant “Multi-field and multi-scale Computational Approach to Design and Durability of PhotoVoltaic Modules” - CA2PVM. JR is also grateful to the support of the Spanish Ministry of Economy and Competitiveness (Projects MAT2015-71036-P and MAT2015-71309-P) and Andalusian Government (Project of Excellence No. TEP-7093).

## A Implementation details

This section succinctly summarizes the discrete form of several operators that are required for the numerical implementation of the current solid shell element.

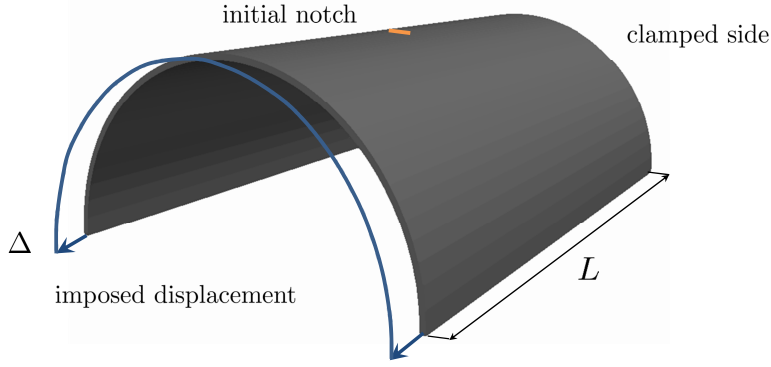


Fig. 18: Cylindrical shell under axial loading: geometry and boundary conditions.

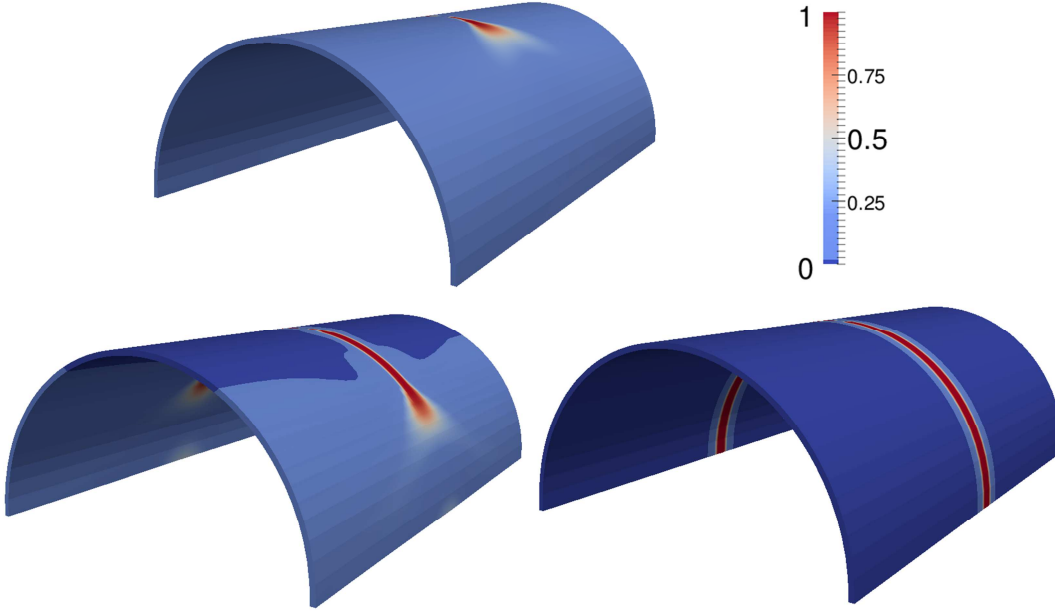


Fig. 19: Cylindrical shell under axial loading: contour plots of the phase field variable.

The discrete version of the curvilinear basis vectors in the current configuration renders:

$$\mathbf{g}_i = \frac{\partial \mathbf{x}}{\partial \xi^i} = \mathbf{G}_i + \frac{\partial \mathbf{u}}{\partial \xi^i} \approx \sum_{I=1}^{n_n} N_{I,\xi^i}(\boldsymbol{\xi}) \begin{bmatrix} X_I \\ Y_I \\ Z_I \end{bmatrix} + \sum_{I=1}^{n_n} N_{I,\xi^i}(\boldsymbol{\xi}) \begin{bmatrix} d_{Ix} \\ d_{Iy} \\ d_{Iz} \end{bmatrix}, \quad \text{with } i = 1, 2, 3, \quad (\text{A.1})$$

where  $N_{I,\xi^i}(\boldsymbol{\xi})$  is the partial derivative of the shape function  $N_I(\boldsymbol{\xi})$  with respect to the natural coordinate  $\xi^i$  and  $n_n = 8$  is the number of nodes. The construction of the compatible displacement-strain  $\mathbf{B}(\mathbf{d})$  operator, Eq.(21), requires the computation of the partial derivative of the covariant basis in the current configuration with respect to the discrete displacements. The general form of the partial derivative of the vectors  $\mathbf{g}_i$  with respect to the displacement vector  $\mathbf{d}_I$  of the node  $I$  is given by

$$\frac{\partial \mathbf{g}_i}{\partial \mathbf{d}_I} = \begin{bmatrix} \frac{\partial g_{ix}}{\partial \mathbf{d}_I} \\ \frac{\partial g_{iy}}{\partial \mathbf{d}_I} \\ \frac{\partial g_{iz}}{\partial \mathbf{d}_I} \end{bmatrix} = \begin{bmatrix} N_{I,\xi^i}(\boldsymbol{\xi}) & 0 & 0 \\ 0 & N_{I,\xi^i}(\boldsymbol{\xi}) & 0 \\ 0 & 0 & N_{I,\xi^i}(\boldsymbol{\xi}) \end{bmatrix}, \quad \text{with } i = 1, 2, 3 \text{ and } I = 1, \dots, n_n. \quad (\text{A.2})$$

The interpolation of the virtual compatible strains is given by

$$\delta \mathbf{E}^u = \sum_{I=1}^{n_n} \mathbf{B}_I(\mathbf{d}) \delta \mathbf{d}_I, \quad (\text{A.3})$$

where  $\delta \mathbf{d}_I$  denotes the virtual nodal displacement vector, whose components are expressed in the global Cartesian setting. Accordingly, the column entries of the strain-displacement operator  $\mathbf{B}_I(\mathbf{d})$  corresponding to the node  $I$  can be expressed as

$$\mathbf{B}_I(\mathbf{d}) = \frac{\partial \bar{\mathbf{E}}}{\partial \mathbf{d}_I} = \begin{bmatrix} \frac{\partial E_{11}^u}{\partial \mathbf{d}_I} \\ \frac{\partial E_{22}^u}{\partial \mathbf{d}_I} \\ \frac{\partial E_{33}^u}{\partial \mathbf{d}_I} \\ 2 \frac{\partial E_{12}^u}{\partial \mathbf{d}_I} \\ 2 \frac{\partial E_{13}^u}{\partial \mathbf{d}_I} \\ 2 \frac{\partial E_{23}^u}{\partial \mathbf{d}_I} \end{bmatrix} = \begin{bmatrix} \mathbf{g}_1^T \frac{\partial \mathbf{g}_1}{\partial \mathbf{d}_I} \\ \mathbf{g}_2^T \frac{\partial \mathbf{g}_2}{\partial \mathbf{d}_I} \\ \mathbf{g}_3^T \frac{\partial \mathbf{g}_3}{\partial \mathbf{d}_I} \\ \mathbf{g}_1^T \frac{\partial \mathbf{g}_2}{\partial \mathbf{d}_I} + \mathbf{g}_2^T \frac{\partial \mathbf{g}_1}{\partial \mathbf{d}_I} \\ \mathbf{g}_1^T \frac{\partial \mathbf{g}_3}{\partial \mathbf{d}_I} + \mathbf{g}_3^T \frac{\partial \mathbf{g}_1}{\partial \mathbf{d}_I} \\ \mathbf{g}_2^T \frac{\partial \mathbf{g}_3}{\partial \mathbf{d}_I} + \mathbf{g}_3^T \frac{\partial \mathbf{g}_2}{\partial \mathbf{d}_I} \end{bmatrix} = \begin{bmatrix} \mathbf{g}_1^T N_{I,\xi^1} \\ \mathbf{g}_2^T N_{I,\xi^2} \\ \mathbf{g}_3^T N_{I,\xi^3} \\ \mathbf{g}_1^T N_{I,\xi^2} + \mathbf{g}_2^T N_{I,\xi^1} \\ \mathbf{g}_1^T N_{I,\xi^3} + \mathbf{g}_3^T N_{I,\xi^1} \\ \mathbf{g}_2^T N_{I,\xi^3} + \mathbf{g}_3^T N_{I,\xi^2} \end{bmatrix}. \quad (\text{A.4})$$

The geometric contribution to the stiffness matrix incorporates the derivative of the B-operator with respect to the kinematic field in order to compute  $\mathbf{S} : \Delta \delta \mathbf{E}^u$ , where  $\Delta \delta \mathbf{E}^u$  identifies the linearized virtual strains. This contribution can be expressed as

$$\mathbf{S} : \Delta \delta \mathbf{E}^u = \delta \mathbf{d} \left[ \left[ \frac{\partial \mathbf{B}(\mathbf{d})}{\partial \mathbf{d}} \right]^T \mathbf{S} \right] \Delta \mathbf{d} = \sum_{I=1}^{n_n} \sum_{K=1}^{n_n} \delta \mathbf{d}_I^T \mathcal{H}_{IK} \Delta \mathbf{d}_K^T, \quad (\text{A.5})$$

with

$$\begin{aligned} \mathcal{H}_{IK} = & S^{11} N_{I,\xi^1} N_{K,\xi^1} + S^{22} N_{I,\xi^2} N_{K,\xi^2} + S^{33} N_{I,\xi^3} N_{K,\xi^3} + S^{12} \left( N_{I,\xi^1} N_{K,\xi^2} + N_{I,\xi^2} N_{K,\xi^1} \right) + \\ & S^{13} \left( N_{I,\xi^1} N_{K,\xi^3} + N_{I,\xi^3} N_{K,\xi^1} \right) + S^{23} \left( N_{I,\xi^2} N_{K,\xi^3} + N_{I,\xi^3} N_{K,\xi^2} \right). \end{aligned} \quad (\text{A.6})$$

Finally, it is nothing that the previous operators should be accordingly modified through the use of the ANS method as detailed in [66].

## References

- Reinoso, J., Paggi, M., Areias, P. (2016) A finite element framework for the interplay between delamination and buckling of rubber-like bi-material systems and stretchable electronics, *Journal of the European Ceramic Society* 36:2371–2382.
- M. Paggi, M. Corrado, M.A. Rodriguez (2013) A multi-physics and multi-scale numerical approach to microcracking and power-loss in photovoltaic modules. *Composite Structures* 95:630–638.
- O. van der Sluis, A.A. Abdallah, P.C.P. Bouten, P.H.M. Timmermans, J.M.J. den Toonder, G. de With (2011) Effect of a hard coat layer on buckle delamination of thin ITO layers on a compliant elasto-plastic substrate: An experimental-numerical approach. *Eng. Fract. Mech.* 78:877–889.
- J.A. Rogers, T. Someya, Y. Huang (2010) Materials and mechanics for stretchable electronics. *Science*. 327:1603–1607.
- M. Jirásek (1998) Nonlocal models for damage and fracture: Comparison of approaches. *Int. J. Solids Struct.* 35:4133–4145.
- J. Lemaitre, J.L. Chaboche (1990) *Mechanics of Solid Materials*, Cambridge University Press, Cambridge. 40:4529–4545.
- R.H.J. Peerlings, R. de Borst, W.A.M. Brekelmans, J.H.P. de Vree (1996) Gradient enhanced damage for quasi-brittle materials. *Internat. J. Numer. Methods Engrg.* 39:3391–3403.
- G. Pijaudier-Cabot, Z. Bazant (1987) Nonlocal damage theory. *J. of Eng. Mech.* 113:1512–1533.
- C. Linder, F. Armero (2007) Finite elements with embedded strong discontinuities for the modeling of failure in solids. *Int. J. Numer. Meth. Engrg.* 72: 1391–1433.
- N. Moës, J. Dolbow, T. Belytschko (1999) A finite element method for crack growth without remeshing, *Int. J. Numer. Methods Engrg.* 46(1):131–150.
- N. Moës, C. Stolz, P.-E. Bernard, N. Chevaugeon (2011) A level set based model for crack growth: thick level set method. *Internat. J. Numer. Methods Engrg.* 86(3):358–380.
- J. Reinoso, M. Paggi (2014) A consistent interface element formulation for geometrical and material nonlinearities. *Comp. Mech.* 54(6):1569–1581.
- S. Forest (2009) Micromorphic approach for gradient elasticity, viscoplasticity, and damage, *J. Engrn. Mech.*, 135:117–131.
- C. Linder, X. Zhang (2013) A marching cubes based failure surface propagation concept for 3D finite elements with non-planar embedded strong discontinuities of higher order kinematics. *International Journal for Numerical Methods in Engineering*. 96:339–372
- T. Waffenschmidt, C. Polindara, A. Menzel, S. Blanco (2014) A gradient-enhanced large-deformation continuum damage model for fibre-reinforced materials. *Comput. Methods Appl. Mech. Eng.* 268:801–842.

16. J. Dolbow , N. Moës , T. Belytschko (2000) Modeling fracture in Mindlin-Reissner with the extended finite element method. *Int J Solids Struct* 33:7161–83.
17. P.M.A. Areias, T. Belytschko (2005) Non-linear analysis of shells with arbitrary evolving cracks using XFEM. *Int. J. Numer. Methods Eng.* 62:384–415.
18. P.M.A. Areias, J.H. Song, T. Belytschko (2006) Analysis of fracture in thin shells by overlapping paired elements. *Comput. Methods Appl. Mech. Eng.* 195:5343–60.
19. T. Rabczuk, P.M.A. Areias (2006) A meshfree thin shell for arbitrary evolving cracks based on an extrinsic basis. *Comput. Model. Eng. Sci.* 16:115–30.
20. T. Rabczuk, G. Zi (2010) A meshfree method based on the local partition of unity for cohesive cracks. *Comput. Mech.* 39(6):743–760.
21. A. Hansbo , P. Hansbo (2004) A finite element method for the simulation of strong and weak discontinuities in solid mechanics. *Comput. Methods Appl. Mech. Eng.* 193:3523–40.
22. T. Chau-Dinh, G. Zi, P.S. Lee, T. Rabczuk, J.H. Song (2012) Phantom-node method for shell models with arbitrary cracks. *Comput Struct* 92:242–56.
23. J.J.C. Remmers, G.N. Wells, R. de Borst (2003) A solid-like shell element allowing for arbitrary delaminations. *Internat. J. Numer. Methods Engrg.* 58:2013–2040.
24. S. Hosseini , J.J. Remmers, R. Borst (2014) The incorporation of gradient damage models in shell elements. *Int. J. Numer. Methods Eng.* 98(6):391–398.
25. L. Ambrosio, V.M. Tortorelli (1992) On the approximation of free discontinuity problems. *Boll. Un. Mat. Ital.* B(7)6(1):105–123.
26. G.A. Francfort, J.J. Marigo (1998) Revisiting brittle fracture as an energy minimization problem. *J. Mech. Phys. Solids* 46(8):1319–1342.
27. H. Amor, J.J. Marigo, C. Maurini (2009) Regularized formulation of the variational brittle fracture with unilateral contact: numerical experiments. *J. Mech. Phys. Solids* 57(8):1209–1229.
28. B. Bourdin, G.A. Francfort, J.J. Marigo (2000) Numerical experiments in revisited brittle fracture. *J. Mech. Phys. Solids* 48(4):797826.
29. A.A Griffith (1921) The phenomena of rupture and flow in solids. *Philos. Trans. Royal Soc. Lond. A* 221:163–198.
30. C. Miehe, M. Hofacker, F. Welschinger (2010) A phase field model for rate-independent crack propagation: robust algorithmic implementation based on operator splits. *Comput. Methods Appl. Mech. Engrg.* 199(45-48):2765–2778.
31. C. Miehe, F. Welschinger, M. Hofacker (2010) Thermodynamically consistent phase field models of fracture: variational principles and multi-field fe-implementations. *Int. J. Numer. Methods Engrg.* 83(10):1273–1311.
32. B. Bourdin, G.A. Francfort, J.J. Marigo (2008) The variational approach to fracture. *J. Elast.* 91(1-3):5–148.
33. C. Miehe L. Schänzel (2014) Phase field modeling of fracture in rubbery polymers. Part I: Finite elasticity coupled with brittle failure. *J. Mech. Phys. Solids* 65:93–113.
34. C. Miehe, L. Schänzel, H. Ulmer (2015) Phase field modeling of fracture in multi-physics problems. Part I. Balance of crack surface and failure criteria for brittle crack propagation in thermo-elastic solids. *Comput. Methods Appl. Mech. Engrg.* 294:449–485.
35. C. Miehe, D. Kienle, F. Aldakheel, S. Teichtmeister (2016) Phase field modeling of fracture in porous plasticity: A variational gradient-extended Eulerian framework for the macroscopic analysis of ductile failure. *Computer Methods in Applied Mechanics and Engineering.* <http://dx.doi.org/10.1016/j.cma.2016.09.028>.
36. X. Zhang, A. Krischok, C. Linder (2016) A variational framework to model diffusion induced large plastic deformation and phase field fracture during initial two-phase lithiation of silicon electrodes. *Computer Methods in Applied Mechanics and Engineering.* <http://dx.doi.org/10.1016/j.cma.2016.05.007>.
37. C. Miehe, L. Schänzel, H. Ulmer (2015) Phase field modeling of fracture in multi-physics problems. Part II. Coupled brittle-to-ductile failure criteria and crack propagation in thermo-elastic-plastic solids *Comput. Methods Appl. Mech. Engrg.* 294:486–522.
38. M.J. Borden, C.V. Verhoosel, M.A. Scott, T. J. R. Hughes, C.M. Landis (2012) A phase field description of dynamic brittle fracture. *Comput. Methods Appl. Mech. Engrg.* 217220:7795.
39. C. Hesch, K. Weinberg (2014) Thermodynamically consistent algorithms for a finite-deformation phase field approach to fracture. *Int. J. Numer. Methods Eng.* 99(12):906-924.
40. M. Hofacker, C. Miehe (2013) A phase field model of dynamic fracture: robust field updates for the analysis of complex crack patterns. *Int. J. Numer. Methods Engrg.* 93(3):276–301.
41. M.A. Keip, B. Kiefer, J. Schröder, C. Linder (2016) Special Issue on Phase Field Approaches to Fracture: In Memory of Professor Christian Miehe (1956-2016). *Comput. Methods Appl. Mech. Engrg.* <http://dx.doi.org/10.1016/j.cma.2016.09.042>.
42. F. Amiri, D. Millán , Y. Shen, T. Rabczuk, M. Arroyo (2014) Phase-field modeling of fracture in linear thin shells. *Theor Appl Fract Mech* 69:102–109.
43. H. Ulmer H, M. Hofacker, C. Miehe (2013) Phase Field Modeling of Fracture in Plates and Shells. *PAMM* 12 (1), 171–172.
44. M. Ambati, L. De Lorenzis (2016) Phase-field modeling of brittle and ductile fracture in shells with isogeometric NURBS-based solid-shell elements. *Computer Methods in Applied Mechanics and Engineering.*
45. P. Areias, T. Rabczuk, M.A. Msekh (2016) Phase-field analysis of finite-strain plates and shells including element subdivision. *Computer Methods in Applied Mechanics and Engineering*, 2016.
46. J. Kiendl, M. Ambati, L. De Lorenzis, H. Gomez, A. Reali (2016) Phase-field description of brittle fracture in plates and shells, *Comput. Methods Appl. Mech. Engrg.* <http://dx.doi.org/10.1016/j.cma.2016.09.011>.
47. M. Bischoff , E. Ramm (1997) Shear deformable shell elements for large strains and rotations. *Int J Numer Methods Eng* 40:4427–4449.
48. R. Hauptmann , K. Schweizerhof (1998) A systematic development of solid-shell element formulations for linear and non-linear analyses employing only displacement degrees of freedom. *Int. J. Numer. Methods Eng.* 42:49–69.
49. S. Klinkel , W. Wagner (1997) A geometrical non-linear brick element based on the EAS-method. *Int. J. Numer. Methods Eng.* 40: 4529–4545.

50. C. Miehe (1998) A theoretical and computational model for isotropic elastoplastic stress analysis in shells at large strains. *Comput. Methods Appl. Mech. Eng.* 155:193–233.
51. J.C. Simo, S. Rifai (1990) A Class of Mixed Assumed Strain Methods and the Method of Incompatible Modes. *Int J Numer Methods Eng* 29:1595–1638.
52. J.C. Simo, F. Armero (1992) Geometrically nonlinear enhanced strain mixed methods and the method of incompatible modes. *Int J Numer Methods Eng* 33:1413–1449.
53. E.N. Dvorkin, K.J. Bathe (1984) Continuum mechanics based fournode shell element for general non-linear analysis. *Eng Comput* 1:77–88.
54. P. Betsch, E. Stein (1995) An assumed strain approach avoiding artificial thickness straining for a nonlinear 4-node shell element. *Commun Numer Methods Eng* 11:899–909.
55. L. Vu-Quoc, X.G. Tan (2003) Optimal solid shells for non-linear analyses of multilayer composites. I. Statics. *Comput. Methods Appl. Mech. Eng.* 192:975–1016.
56. M.A. Msekh, M. Sargado, M. Jamshidian, P. Areias, T. Rabczuk (2015) Abaqus implementation of phase field model for brittle fracture. *Comput. Mater. Sci.* 96(B):472–484.
57. R. Hauptmann, K. Schweizerhof, S. Doll (2000) Extension of the solid-shell concept for application to large elastic and large elastoplastic deformations. *Int. J. Numer. Methods Eng.* 49:1121–1141.
58. M. Schwarze, S. Reese (2011) A reduced integration solid-shell finite element based on the EAS and the ANS concept—large deformation problems. *Int. J. Numer. Methods Eng.* 85:289–329.
59. G. Holzapfel (2000) *Nonlinear solid mechanics*. John Wiley & Sons Ltd. ISBN: 978-0-471-82319-3.
60. K. Rah, W. Van Paeppegem, A.M. Habraken, J. Degrieck, R.A. de Sousa, R.A.F. Valente (2013) Optimal low-order fully integrated solid-shell elements. *Comput Mech* 51(3):309326.
61. Büchter N, Ramm E, Roehl D. (1994) Three-dimensional extension of nonlinear shell formulation based on the enhanced assumed strain concept. *Int J Numer Meth Engng* 37:2551-2568.
62. O.C. Zienkiewicz, R.L. Taylor (2000) *The Finite Element Method*. Butterworth-Heinemann, Woburn, MA, 5th Edition, Vol. I. ISBN: 0750650494.
63. Reinoso, J., Blázquez, A. (2016) Application and finite element implementation of 7-parameter shell element for geometrically nonlinear analysis of layered CFRP composites, *Composite Structures* 139:263–276.
64. J.C. Simo, F. Armero, R.L. Taylor (1993) Improved versions of assumed enhanced strain tri-linear elements for 3D finite deformation problems. *Comput Meth Appl Mech Engng* 110(3):359–386.
65. N. Hocine, M. Abdelaziz, A. Imad (2022) Fracture problems of rubbers: J-integral estimation based upon factors and an investigation on the strain energy density distribution as a local criterion. *International Journal of Fracture*, 117:1-23.
66. Klinkel S, Wagner W. (1997) A geometrical nonlinear brick element based on the easmethod. *International Journal for Numerical Methods in Engineering* 40: 4529–4545.